DOI: 10.26599/FSHW.2026.9250948

Contents lists available at SciOpen

Food Science and Human Wellness

journal homepage: https://www.sciopen.com/journal/2097-0765

China Food Publishing Co.

Protective Effect of Peach Gum Polysaccharides on Alcohol-Induced Liver Injury via the Gut Liver Axis

Yue Cao[1], Yue Lu[1], Mengyuan Chen[1], Yuanren Zhu[1], Xiao Guo[1], Qing Yang[1], Min Fang[1], Yongning Wu[2] and Zhiyong Gong[1,*]

[1] *Key Laboratory for Deep Processing of Major Grain and Oil, Ministry of Education, College of Food Science and Engineering, Wuhan Polytechnic University, Wuhan 430023, Hubei, China.*

[2] *NHC Key Laboratory of Food Safety Risk Assessment, Food Safety Research Unit (2019RU014) of Chinese Academy of Medical Science, China National Center for Food Safety Risk Assessment, Beijing 100021, China.*

ABSTRACT: Disrupted intestinal homeostasis exacerbates alcoholic liver disease (ALD) via the gut-liver axis. While our previous study has demonstrated peach gum polysaccharides (PGPs) alleviate ALD through antioxidant and lipid metabolism regulation, their protective effects on the intestinal barrier remain unexplored. Here, three polysaccharide fractions (PGP40, PGP60, PGP80) were extracted using stepwise ethanol precipitation. Structural characterization revealed that all fractions were β-pyranose-type arabinogalactans, with PGP80 possessing the lowest molecular weight and most potent scavenging activity against DPPH, ABTS, and •OH radicals. In Lieber-DeCarli diet-induced ALD mice, PGP80 supplementation significantly attenuated hepatic lipid accumulation and oxidative stress, and reduced levels of pro-inflammatory cytokines. Crucially, it restored intestinal barrier function by reducing intestinal permeability and enhancing tight junction proteins (ZO-1, Occludin). PGP80 concurrently modulated gut microbiota composition, suppressing detrimental taxa (*Verrucomicrobia*, *Rikenella*) while enriching short-chain fatty acid (SCFA)-producing genera (*Dubosiella*, *Ligilactobacillus*, *Prevotellaceae UCG-001*). The resulting increase in SCFAs enhanced intestinal epithelial barrier integrity, thereby decreasing systemic translocation of lipopolysaccharide (LPS) and D-lactic acid. This cascade culminated in improved hepatic metabolic homeostasis and attenuated inflammation, potentially involving the gut-liver axis. Our findings suggest that PGP80 ameliorate ALD, at least partially through gut-liver axis modulation, thereby broadening the application value of peach gum.

Keywords: Peach gum polysaccharide; Chronic alcoholic liver disease; Gut microbiota; Gut liver axis

1. Introduction

With improving socioeconomic conditions, shifting dietary patterns, and increasing alcohol consumption frequency, the incidence of alcohol-associated disorders has risen steadily. Alcoholic liver disease (ALD) has now emerged as the second leading cause of global liver disease burden, surpassed only by viral hepatitis [1]. Epidemiological studies reveal that approximately 70% of individuals with chronic alcohol abuse develop hepatic steatosis, 20%-30% progress to alcoholic steatohepatitis, and 10% advance to irreversible cirrhosis [2].

***Corresponding author**
gongwhqg@163.com

Received 29 April 2025
Received in revised from 12 June 2025
Accepted 9 October 2025

Early therapeutic strategies for ALD primarily targeted the mitigation of alcohol-induced hepatic oxidative stress and inflammatory cascades [3]. Nevertheless, accumulating evidence demonstrates that chronic alcohol consumption induces intestinal dysbiosis, subsequently triggering intestinal barrier dysfunction [4]. Experimental studies by Yan et al. revealed that pathogen-associated molecular patterns (PAMPs), particularly lipopolysaccharide (LPS), migrate into the portal circulation and hepatic tissue. Circulating LPS binds to endotoxin receptors, activating hepatic TLR4 signaling pathways, which subsequently stimulate Kupffer cells to generate excessive reactive oxygen species (ROS). This ROS overproduction triggers hepatocyte oxidative stress. Such a cascade based on gut liver axis established a close relationship between oxidative stress and the liver LPS/TLR4 pathway and was considered to be a key event contributing to the pathogenesis of ALD. [5]. Furthermore, investigations in chronic ALD models revealed a significant increase in the relative abundance of *Bacteroidetes* alongside a marked decrease in unclassified *Lachnospiraceae*, indicative of gut microbial dysbiosis. This disruption in gut microbiota was accompanied by a thinned mucus layer, reduced goblet cell population, compromised intercellular tight junctions, and diminished antimicrobial peptide production. This exacerbates endotoxin leakage, promoting LPS-mediated activation of the TLR4/NF-κB signaling pathway, which in turn aggravates hepatic lipid accumulation and inflammatory injury. [6]. The gut-liver axis has been mechanistically validated as a pivotal pathogenic pathway in ALD development. Although drugs exhibiting anti-inflammatory and anti-fibrotic properties (e.g., glucocorticoids and silymarin) are employed in alcoholic steatohepatitis management, their therapeutic application is limited by progressively accumulating adverse effects and substantial cost burdens during chronic administration [7]. To date, no therapeutic approach beyond alcohol abstinence has proven effective in halting the progression of ALD. Consequently, identifying natural compounds with dual antioxidant and microbiota-regulating capabilities emerges as a critical research priority for ALD management.

Peach gum (PG) is a translucent, amber-colored, stress-induced natural plant-based gum exudate secreted from the branches of peach trees (Prunus persica (L.) Batsch, Rosaceae family) following exposure to physical or chemical stimuli [8]. Typically, PG primarily consists of a macromolecule polysaccharide characterized by (1→3)- and (1→6)-linked β-D-galactopyranose (Galp) backbones with highly branched structures [9]. The highly branched macromolecular structure of peach gum polysaccharides (PGPs) contains abundant active functional groups such as hydroxyl (-OH), which can directly scavenge reactive oxygen species (ROS) by donating hydrogen atoms to terminate free radical chain reactions, thereby exerting antioxidant activity [10]. Accumulating evidence demonstrates that PGPs possess multiple bioactive properties, including immunomodulatory effects, antioxidant capacities, antimicrobial activities [11], anti-inflammatory efficacy, hypoglycemic and hypolipidemic effects, alcohol-induced hepatic injury alleviation, and gut microbiota-regulating capabilities [12]. Our previous investigations have demonstrated that the administration of PGPs exerts hepatoprotective effects through modulation of D-glutamate metabolism, alanine aspartate glutamate pathways, and arginine biosynthesis. This metabolic regulation reduces oxidative stress biomarkers and downregulates proinflammatory cytokines (TNF-α, IL-6 and IL-1β) in acute alcohol-induced liver injury

mouse model [13]. The hepatoprotective mechanism of PGPs against ALD might be associated with the regulation of oxidative stress and lipid metabolism. However, systematic investigations into the hepatoprotective effects of PGPs against chronic ALD through the gut-liver axis and their underlying mechanisms remain unexplored. Futhermore, research has reported significant differences in the bioactivity of polysaccharides based on molecular weight. For instance, lower molecular weight *Tremella fuciformis* polysaccharides exhibit stronger antioxidant and immunomodulatory activities than their higher molecular weight counterparts [14]. Similarly, *Polygoni Multiflori Radix Praeparata* polysaccharides of varying molecular weights demonstrate distinct anti-aging activities [15]. While research exists on the anti-inflammatory and antioxidant activities of crude PGPs, it remains unclear which molecular weight fractions confer superior activity. Therefore, we employed stepwise ethanol precipitation, a method widely used in polysaccharide research to separate fractions of different molecular weights and bioactivities [16], to prepare distinct molecular weight PGPs for comparative structural and bioactivity analysis.

In this study, we isolated distinct PGPs fractions (PGP40, PGP60 and PGP80) from PG using stepwise ethanol precipitation, conducted structural and bioactive characterization while establishing a chronic alcohol-induced liver injury murine model. The investigation focused on evaluating PGP80's effects on hepatic damage, intestinal barrier integrity, and gut microbiota homeostasis in ALD mice. Mechanistic insights into PGP80's hepatoprotective effects against ALD were elucidated via the gut-liver axis regulatory paradigm. This study systematically deciphers the molecular mechanisms underlying peach gum polysaccharides' protective effects against alcohol-induced hepatotoxicity and provides a theoretical foundation for developing natural polysaccharide based functional foods to alleviate ALD symptoms.

2. Materials and methods

2.1 Materials and reagents

Raw peach gum powder was provided by Suizhou Peach Gum Industry, Hubei, China. Methanol, trichloroacetic acid, and trifluoroacetic acid (chromatographic grade) were obtained from Merck KGaA (Darmstadt, Germany). Trichloromethane, anhydrous ethanol, sulfuric acid, and monosaccharides standards were obtained from Sinopharm Chemical Reagent Co., Ltd. (Shanghai, China). Occludin, ZO-1 and GAPDH antibodies were obtained from ABclonal (Wuhan, China). All chemicals and reagents utilized in this study were of analytical grade. The Lieber-DeCarli liquid diet was obtained from Trophic Animal Feed High-Tech Co., Ltd (China), and the nutritional composition of experimental diets is detailed in Supplementary Table S1.

Biochemical assay kits were obtained from Nanjing Jiancheng Bioengineering Institute (Nanjing, China). Enzyme-linked immunosorbent assay (ELISA) kits were acquired from Jingmei Biological Technology Co., Ltd. (Jiangsu, China).

2.2 Preparation of PGPs

The procedure for extracting peach gum polysaccharides using stepwise ethanol precipitation [17] is illustrated in Fig. 1A. Specifically, after passing through a 100-mesh sieve, the raw peach gum powder was

mixed with Milli-Q water at a ratio of 1:100 (w/v), stirred at 90°C for 2 h, subjected to dual extraction cycles, and centrifuged at 4000 rpm for 15 min. The supernatant was concentrated to 1/5 of its original volume by rotary evaporation. The concentrated supernatant was supplemented with absolute ethanol to achieve 40% (v/v) ethanol concentration. After overnight precipitation at 4°C, the resulting precipitate was collected by centrifugation and designated as crude PGP40. The supernatant was subsequently subjected to sequential ethanol precipitation by adjusting ethanol concentrations to 60% and 80% (v/v) using the same protocol, yielding crude PGP60 and PGP80 precipitates respectively. All three crude polysaccharide fractions were redissolved in Milli-Q water at a ratio of 1:25 (g/mL) and deproteinized with Sevage reagent (chloroform:n-butyl alcohol = 4:1, v/v). Dialysis was carried out using membranes with a molecular weight cutoff of 14 kDa for 48 h, followed by lyophilization to obtain three purified peach gum polysaccharide fractions: PGP40, PGP60, and PGP80.

2.3 Characterization of PGPs

The extraction yields of various PGPs fractions were quantified using equation (1). Carbohydrate content in PGPs was determined via the phenol-sulfate method with glucose as the standard.

$$\text{Extraction rate} = \frac{\text{Quality of lyophilized PGPs (g)}}{\text{Quality of peach gum powder (g)}} \times 100\% \quad (1)$$

The molecular weight distribution of PGPs was characterized using high performance gel permeation chromatography (HPGPC) [18]. Monosaccharide constituents were analyzed via high-performance ion exchange chromatography (HPIEC) (Dionex ICS 5000+ system, USA) following the protocol established by Wang et al. [19].

PGPs samples (2 mg) were homogenously blended with 200 mg KBr under infrared drying conditions, followed by FTIR spectral acquisition in the 4000-400 cm^{-1} range using a PerkinElmer Fourier-transform infrared spectrometer (USA). UV-Vis absorption profiles were recorded from 190 to 400 nm using a Thermo Scientific spectrophotometer (USA). The spatial conformation of PGPs was characterized through Congo red binding assays and X-ray diffraction (XRD) analysis following the methodology described by Wang et al. [20]. Particle size distribution was determined using a laser diffraction analyzer (Mastersizer 3000, Malvern Instruments Ltd., USA). Prior to scanning electron microscopy (SEM) observation, polysaccharide samples were subjected to gold sputtering using an ion sputter coater and critical point drying. The prepared specimens were subsequently mounted onto scanning electron microscope stages and imaged under high-vacuum conditions.

2.4 Antioxidant activity of PGPs

The in vitro antioxidant activity assay of peach gum polysaccharides was optimized based on previously established laboratory protocols and conducted as detailed below [13].

2.4.1 2-Diphenyl-picryl hydrazine free radical (DPPH) scavenging ability

PGPs solutions (1-10 mg/mL) were prepared. Subsequently, 0.2 mL of DPPH radical solution (0.4 mol/L in anhydrous ethanol) and 2 mL deionized water were sequentially added to 1.0 mL PGPs solution. The

mixture was homogenized and kept in darkness for 30 min at room temperature. A control group (deionized water replacing PGPs solution) was established as reference, and absorbance was measured at 517 nm. Vitamin C served as the positive control.

$$\text{DPPH scavenging ability} = \left[1 - \frac{(A_1 - A_2)}{A_0}\right] \times 100\% \quad (2)$$

where A_0 denotes the blank control absorbance (deionized water substituting PGPs solution), A_1 corresponds to the absorbance of the complete reaction system, and A_2 indicates the absorbance of the test system with DPPH solution replaced by deionized water.

2.4.2 Hydroxyl radical (·OH) scavenging ability

To 2 mL of PGPs solution (1-10 mg/mL), 2 mL $FeSO_4$ (6 mmol/L), 2 mL H_2O_2 (6 mmol/L), and 2 mL salicylic acid (6 mmol/L) were sequentially supplemented. Following 30-min incubation at ambient conditions, absorbance was recorded at 510 nm. Vitamin C served as the positive control.

$$\cdot\text{OH scavenging ability} = \left[1 - \frac{(A_1 - A_2)}{A_0}\right] \times 100\% \quad (3)$$

where A_0 denotes the blank control absorbance (deionized water substituting PGPs solution), A_1 corresponds to the absorbance of the complete reaction system, and A_2 indicates the absorbance of the test system with H_2O_2 replaced by deionized water.

2.4.3 ABTS radical scavenging activity

PGPs solutions (1-10 mg/mL) were prepared. The ABTS radical cation ($ABTS^{+}$•) working solution was prepared by combining equimolar volumes of 7.4 mM ABTS and 5 mM $K_2S_2O_8$. Following 16-hour dark incubation, the mixture was adjusted with ethanol to achieve A_{734} nm = 0.70 ± 0.02. For the assay, a fixed volume (1.8 mL) of the $ABTS^{+}$• working solution was mixed with different volumes of the PGPs solutions (corresponding to final concentrations in the reaction mixture ranging from 0.1 to 1.0 mg/mL). Ethanol was then added to bring the total reaction volume to 2.0 mL. After thorough mixing, the reaction proceeded for 10 min at room temperature, followed by absorbance measurement at 734 nm using ethanol as blank.

$$\text{ABTS radical scavenging ability} = \left[1 - \frac{(A_1 - A_2)}{A_0}\right] \times 100\% \quad (4)$$

where A_0 denotes the blank control absorbance (deionized water substituting PGPs solution), A_1 corresponds to the absorbance of the complete reaction system, and A_2 indicates the absorbance of the test system with ABTS replaced by deionized water.

2.5 Hepatoprotective effects of PGP80 against ALD

2.5.1 Animal experiments and agent administration protocol

A total of 72 male C57BL/6J mice (7-8 weeks old, 18-22 g) were obtained from Hunan SJA Laboratory Animal Co., Ltd (Hunan, China; animal production license number SCXK (XIANG) 2024-0009). Mice were

housed under specific pathogen-free conditions maintained at 25 ± 1°C with 60-70% relative humidity and a 12-hour light/dark cycle. After 1 week of adaptive feeding, animals were randomly allocated into six groups (n=12 per group): liquid diet control (Con), model control (Mod), positive drug control (Pos), and three PGP80 intervention groups (PGP80-L, PGP80-M, PGP80-H). A modified Gao-Binge protocol was implemented for chronic alcoholic liver injury induction [21]. All mice received a 7-day acclimatization period with Lieber-DeCarli control liquid diet, followed by gradual transition to ethanol-containing Lieber-DeCarli diet over 1 week (Supplementary Fig. S1.) Experimental groups (Mod, PGP80 intervention, and Pos group) were then maintained for 8 consecutive weeks on a liquid diet containing 4% (v/v) ethanol, with the ethanol accounting for 28% of the total dietary calories. To ensure isocaloric intake between groups, a staggered feeding protocol was employed where control groups received daily rations equivalent to the previous day's ethanol diet consumption by experimental counterparts.

From week 5 onward, Pos group received daily oral administration of 150 mg/kg bifendate, while PGP80 intervention groups were administered 200, 400, or 600 mg/kg PGP80 solutions respectively, and equal amounts of 0.9% normal saline were given to the Con and Mod group. All treatments were administered before 09:00 daily for 4 weeks. Fecal samples were collected from mice one day prior to experimental termination, immediately flash-frozen in liquid nitrogen, and stored at -80°C for subsequent analyses. Twenty-four hours prior to termination, Mod, PGP80 intervention and Pos group received a 31.5% (v/v) ethanol binge (5 ml/kg), with Con group receiving isocaloric maltodextrin solution. Following overnight fasting, experimental mice were anesthetized via chloroform inhalation followed by euthanasia with subsequent collection of blood samples, liver tissues, and ileal segments. All experimental protocols were approved by the Animal Welfare Ethics Committee of Wuhan Polytechnic University (Approval No. WPU202410008) in strict compliance with institutional guidelines for laboratory animal care. The detailed methodology for establishing the mouse model of chronic alcohol-induced liver injury is illustrated in Fig. 1B.

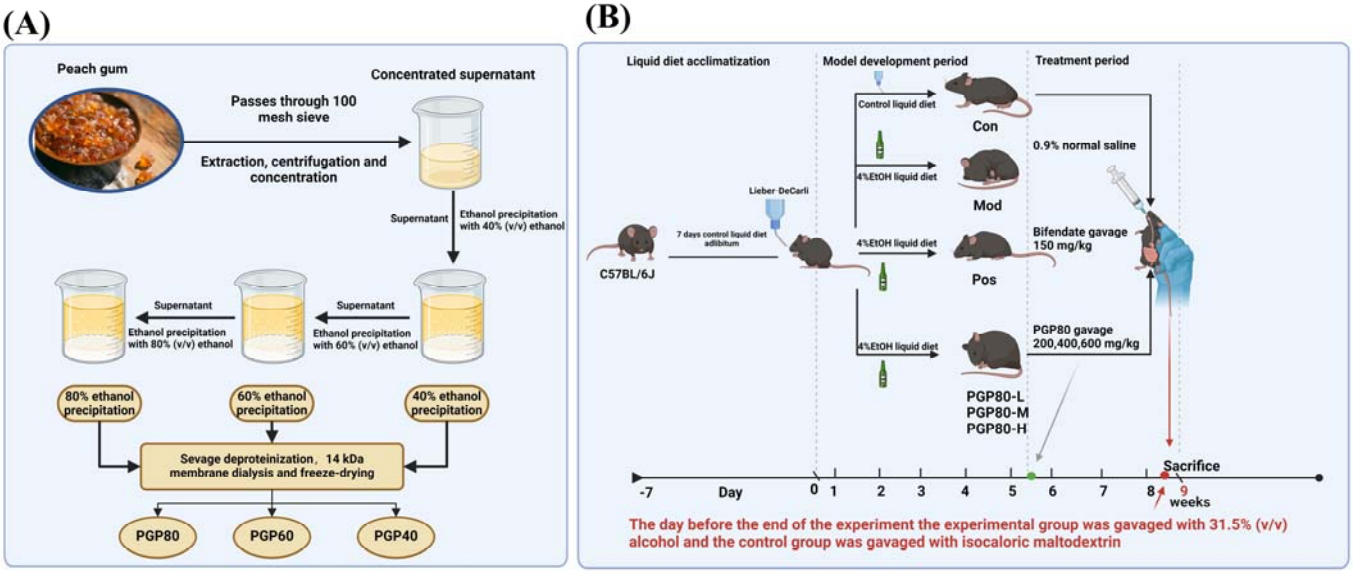

Figure 1: Extraction of PGPs and ALD modeling intervention protocol. (A) Stepwise ethanol precipitation protocol for PGPs extraction. (B) Research protocol investigating the hepatoprotective mechanisms of PGP80 against ALD. The 4% EtOH (v/v) liquid diet contained ethanol at a concentration providing 28% of the total dietary calories.

2.5.2 Animal mortality monitoring

During the animal model establishment phase, six mice (out of 72 total modeled mice, including 12 reserve animals) died in the gradual transition period to ethanol-containing liquid diet (stepwise increase of ethanol-derived calories). The mortality was attributed to: lethal malnutrition due to insufficient intake caused by individual variations in ethanol aversion, where these animals rejected the ethanol-supplemented liquid diet. These subjects were excluded from the final analysis. All deaths occurred within the first 4 weeks of modeling. Since 12 reserve mice were prepared in advance using identical modeling procedures, this mortality did not impact the final experimental outcomes. All procedures complied with IACUC-specified humane endpoints (Protocol No. WPU202410008).

2.5.2 Biochemical assays

Animal food intake was meticulously monitored on a daily basis, and body weight changes were recorded through biweekly measurements. The hepatic index was calculated as the ratio of the precisely measured liver wet weight to the body weight of the mice.

Liver tissue was mixed with precooled saline at a 1:9 mass-to-volume ratio and homogenized using a high-throughput tissue grinder. Blood samples were centrifuged at 3000 rpm for 10 minutes (4°C) to collect the supernatant serum. Serum levels of ALT, AST, TC, TG, HDL-C, LDL-C, TNF-α, IL-1β, LPS and D-lactic acid were quantified using analytical kits and ELISA kit. Hepatic homogenates were analyzed for oxidative stress markers (GSH, MDA, SOD), alcohol-metabolizing enzymes (ADH, ALDH) with commercial assay kits.

2.5.3 Histopathological observation

Liver tissue specimens (5 mm × 5 mm × 3 mm) were harvested from the middle-left hepatic lobe of murine subjects and immersion-fixed in 4% paraformaldehyde (PFA) for subsequent histological processing, including hematoxylin-eosin (H&E) staining and Oil Red O lipid visualization. Ileal tissue Ileal tissue segments (1 cm in length) were fixed in 4 PFA, processed into paraffin-embedded blocks, and sectioned for subsequent histological analysis via H&E staining. Ileum tissue sections were deparaffinized, antigen-retrieved, and treated with peroxidase blocker (10 min) and protein blocker (10 min). Primary antibodies (ZO-1/Occludin, 1:200) were applied for 2 h, followed by secondary IgG polymer (10 min), streptavidin-HRP (15 min), and DAB staining (10 min, dark). Sections were counterstained with hematoxylin, dehydrated, cleared in xylene, and mounted for immunohistochemical (IHC) examination. Hepatic lipid deposition in Oil Red O-stained sections was quantified using Fiji ImageJ software. Histochemistry score (H-Score) semiquantitative analysis was performed by using the Aipathwell® digital pathology image analysis system to evaluate tight junction protein expression in ileal immunohistochemical sections. The specific workflow was as follows: For intestinal tissue, the mucosa layer was preferentially selected as the region of analysis. Based on the HSI color model (Hue, Saturation, Intensity), positive staining was classified into intensity grades: weak positive (light yellow, score 1), moderate positive (brown-yellow, score 2), and strong positive (dark brown, score 3). Subsequently, the software automatically identified nuclei and

expanded the region to the cytoplasmic compartment. It simultaneously quantified the number, area, and integrated optical density (IOD) of weakly, moderately, and strongly positive cells, while also recording parameters such as total tissue area. It was calculated using the following formula:

$$H-S\text{core}=\sum(p_i\times i)=(p_{\text{Weakly positive}}\times 1)+(p_{\text{Moderately positive}}\times 2)+(p_{\text{Strongly positive}}\times 3) \quad (4)$$

where: i represents the intensity grade score (Negative: 0; Weak positive: 1; Moderate positive: 2; Strong positive: 3); p_i represents the percentage (%) of cells at the corresponding intensity grade. The score ranges from 0 to 300. A higher score indicates a greater combined expression level of both the proportion of positive cells and the staining intensity within the tissue sample.

2.5.4 Western blotting

Total protein was isolated from tissues using Radio-Immunoprecipitation Assay (RIPA) lysis buffer (Beyotime Biotechnology, Shanghai, China) supplemented with protease and phosphatase inhibitor cocktail. Tissue homogenates were centrifuged at 14,000 × *g* for 20 min at 4°C. Protein concentration was determined by bicinchoninic acid (BCA) assay. Equal amounts of protein (50 μg per lane) were separated by SDS-polyacrylamide gel electrophoresis (SDS-PAGE) and subsequently transferred onto 0.22-μm polyvinylidene difluoride (PVDF) membranes (Millipore, Merck KGaA, Germany). Membranes were blocked with 5% non-fat milk in Tris-buffered saline containing 0.1% Tween-20 (TBST) for 2 h at 28°C, followed by incubation with primary antibodies overnight at 4°C. Protein bands were visualized using enhanced chemiluminescence (ECL) reagent (CLINX, Shanghai, China) and imaged with a chemiluminescence detection system. Subsequently, appropriate images were selected and the optical density values of target bands were analyzed using the AlphaEaseFC software processing system.

2.5.5 Short-chain fatty acids (SCFAs) detection

Fecal samples (50 mg) were homogenized in 500 μL ice-cold PBS (0.5% v/v) with zirconium beads using a high-throughput tissue grinder (two cycles: 50 Hz, 5 min/cycle, liquid nitrogen cooling), followed by 10-min ultrasonication. After centrifugation (13,000×g, 15 min, 4°C), supernatants underwent liquid-liquid extraction with n-butanol containing 2-ethylbutyric acid (internal standard), involving vortex mixing (10 s), low-temperature ultrasonication (10 min), and final centrifugation (15,000×g, 5 min, 4°C). Calibration standards (acetic, propionic, butyric, isobutyric, isovaleric and valeric acids) and internal standard solutions were prepared in HPLC-grade n-butanol through serial dilution (1-100 μg/mL with 1 μg/mL internal standard). GC analysis was conducted on an Agilent 7890B system equipped with HP-FFAP capillary column (30 m×0.25 mm×0.25 μm) under helium flow. Oven temperature program: 80°C (1 min) → 10°C/min → 220°C (5 min). Injection parameters: 1 μL splitless mode, 250°C inlet, 300°C FID. Serum samples (100μL), add 500μL water and mix well, add 300μL 50% sulfuric acid, then add 100μL of 500mg/L internal standard (cyclohexanone) solution and 2mL diethyl ether, homogenize for 1min, centrifuge at 4℃ 12,000 rpm for 10min, take the supernatant for analysis using GCMS QP2010-Ultra. Chromatographic system: Agilent DB-WAX capillary column (30 m × 0.25 mm × 0.25 μm); carrier gas: high-purity helium (purity ≥ 99.999%), flow rate 1.0 mL/min; inlet temperature 220℃, injection volume 1μL, splitless injection, solvent delay time

2.5min. Mass spectrometric system: electron impact (EI) ion source, ion source temperature 230℃, interface temperature 220℃.

2.5.6 16S rRNA gene sequencing analysis

The total microbial genomic DNA was extracted from fecal specimens using the E.Z.N.A.® Soil DNA Kit (Omega Bio-tek, Norcross, GA, USA). The hypervariable V3-V4 region of bacterial 16S rRNA genes was amplified using primer pair 341F (5'-CCTACGGGNGGCWGCAG-3') and 805R (5'-GACTACHVGGGTATCTAATCC-3'). Raw sequencing reads were processed through quality control pipelines involving read merging and filtering to generate high-quality sequences. Operational taxonomic units (OTUs) were delineated at 97% sequence similarity using the UPARSE algorithm (version 7.1). Sequencing libraries were prepared following manufacturer's protocols and subjected to paired-end sequencing (2×300 bp) on an Illumina MiSeq platform (Majorbio Bio-pharmaceutical Technology Co., Ltd., Shanghai, China) using PE300 chemistry.

2.6 Statistical analysis

Experimental data were expressed as mean ± standard deviation (SD). All statistical comparisons among three or more groups were performed using Tukey's post hoc test following one-way ANOVA by using SPSS Statistics 26.0 software (IBM Corp.). Data visualizations were generated with OriginPro 2025 (OriginLab Corporation) and GraphPad Prism 9 (GraphPad Software). The letters marked on the bar chart (e.g., a, b, ab, c, etc.) denote statistically significant differences ($P < 0.05$) among groups, whereas groups sharing the same letter are not significantly different ($P > 0.05$). Gut microbiota bioinformatic analysis was conducted using the Majorbio Cloud platform (https://cloud.majorbio.com).

3. Results and Discussion

3.1 Characterization of PGPs

The yield, carbohydrate, and monosaccharide composition of different fractions are presented in Table 1. PGP80 exhibited the highest yield and carbohydrate at 35.94 ± 2.19% and 86.10 ± 5.19%, respectively. All three PGPs fractions were heteropolysaccharides composed of seven monosaccharides: Ara, Rha, Gal, Glu, Xyl, Man, and Glu-UA, with Ara and Gal demonstrating the highest relative proportions. HPGPC analysis revealed that PGP40, PGP60, and PGP80 each contained three distinct fractions, with PGP80 displaying the lowest average molecular weight of 2.76×10^6 (Supplementary Table S2 and Fig. S2). This effect likely arises because high ethanol concentrations compete with polysaccharides for surface binding, reducing their water solubility and inducing aggregation, thereby improving extraction efficiency and carbohydrate retention [22]. Studies have demonstrated that the pronounced antioxidant activity of natural bioactive polysaccharides shows significant correlations with lower molecular weight and elevated Gal content [23]. These findings help identify the antioxidant components of polysaccharides and lay a structural foundation for studying their molecular mechanisms in bioactivities, such as intestinal metabolism and free radical scavenging.

Table 1. Yield, carbohydrate and monosaccharide composition of three polysaccharide fractions.

	PGP40	PGP60	PGP80
Yield (%)	16.03±2.06^{c}	30.00±4.61^{b}	35.94±2.19^{a}
Carbohydrate (%)	75.36±7.50^{b}	83.27±6.67^{ab}	86.10±5.19^{a}
Monosaccharide composition (%)			
Ara	44.47	44.41	44.5
Rha	1.39	1.39	1.32
Gal	34.51	34.6	34.54
Glu	0.27	0.23	0.29
Xyl	12.61	12.59	12.65
Man	3.37	3.32	3.31
Glu-UA	3.74	3.45	3.39

Yield was calculated based on dry powders of raw peach gum powder. Data are shown as mean ± S.D (n=6). Statistical significance was determined using ANOVA, complemented by a post-hoc Tukey's test to discern specific differences among the groups. Values with different letters in the same column are significantly different ($P < 0.05$).

Fig. 2A and B present the UV-Vis absorption and FT-IR spectra of the three polysaccharide fractions, respectively. The absence of distinct absorption peaks at 260 nm (nucleic acid specific wavelength) and 280 nm (protein specific wavelength) in all fractions confirms that the purified products meet the purity standards for natural product chemistry studies, establishing a robust foundation for subsequent structural characterization and bioactivity evaluation. The FT-IR spectra of PGP40, PGP60, and PGP80 showed nearly identical profiles: a strong broad absorption peak at 3404.91 cm^{-1} was attributed to O–H stretching vibrations from hydroxyl group in saccharide rings and their hydrogen-bonding networks, with peak intensity reflecting high hydroxyl content [24]; a weak absorption band at 2924.43 cm^{-1} corresponded to C–H symmetric stretching vibrations characteristic of polysaccharides [25]; the 1613.03 cm^{-1} peak indicated O–H bending vibrations of bound water molecules, signifying polysaccharide-water hydrogen bonding [26]; the intense 1044.39 cm^{-1} peak was assigned to asymmetric C–O–C stretching in pyranose rings, while the 607.99 cm^{-1} ring-breathing vibration further corroborated the pyranose conformation [27]; and the 887.90 cm^{-1} absorption suggested β-glycosidic linkages [28]. Collectively, these spectral signatures demonstrate that PGP40, PGP60, and PGP80 are β-glycosidically linked pyranose-type polysaccharides.

The triple-helical configuration, as a representative ordered conformation, has been experimentally validated to significantly potentiate polysaccharide bioactivity. Helical structures in polysaccharides arise from ordered β-(1→3)-glycosidic linkages. This configuration enhances antioxidant activity by improving electron transfer and stabilizing free radicals [29]. Fig. 2C shows that all three polysaccharide fractions displayed bathochromic shifts under increasing NaOH concentrations, confirming their stable triple-helical structures. XRD patterns of the fractions within the 2θ range of 4°-60° displayed broadened diffuse scattering maxima (Fig. 2D), suggesting amorphous polymeric states. Notably, this non-crystalline characteristic appears contradictory to the helical configuration identified in Congo red assays, though similar phenomena have been reported in studies of *Lentinan* where non-crystalline polymers demonstrated localized ordered triple helices [30]. This paradox may arise from dynamic ordered microdomains stabilized through

intermolecular hydrogen bonding, while maintaining global amorphous aggregation. Such unique "order-disorder" coexistence architecture may constitute the structural basis for the distinctive bioactivities of peach gum polysaccharides.

SEM and particle size analysis revealed distinct morphological differences among PGP40, PGP60, and PGP80 (Supplementary Table S3 and Fig. S3). The PGP40 exhibited relatively smooth flake-like structures, while both PGP60 and PGP80 displayed irregular porous morphologies with pronounced surface wrinkles and undulations. Particle size distribution analysis demonstrated that the PGP80 fraction possessed the smallest characteristic particle size (D_{50} = 64.20 ± 1.80 μm) and exhibited superior monodispersity (Span = 1.45 ± 0.05) compared to the other two fractions.

3.2 Antioxidant activity assays of PGPs in vitro

Excessive accumulation of free radicals has been strongly associated with the pathogenesis of multiple hepatic disorders. In vitro antioxidant assays can be used to preliminarily screen for polysaccharides with higher antioxidant potential. As illustrated in Fig. 2E-H, all polysaccharide fractions demonstrated significant in vitro antioxidant activity, with enhanced radical-scavenging capacity corresponding to increasing ethanol concentrations. The IC_{50} values for PGP40 were determined as (4.23 ± 0.16) mg/mL (DPPH), (5.68 ± 0.19) mg/mL (ABTS), and (4.46 ± 0.14) mg/mL (•OH). PGP60 exhibited intermediate scavenging activity, showing IC_{50} values of (3.36 ± 0.19) mg/mL for DPPH, (4.53 ± 0.21) mg/mL for ABTS, and (3.72 ± 0.24) mg/mL for •OH. Notably, PGP80 displayed the most potent antioxidant effects, with significantly lower IC_{50} values of 2.61 ± 0.12 mg/mL (DPPH), 3.66 ± 0.08 mg/mL (ABTS), and 2.71 ± 0.19 mg/mL (•OH) ($P < 0.05$ compared to both PGP40 and PGP60). This progressive decrease in IC_{50} values with higher ethanol concentrations indicates a concentration-dependent enhancement of antioxidant capacity among the polysaccharide fractions. Notably, Zhou et al. [13] reported dose-dependent antioxidant effects of PGPs in vitro, consistent with our findings. Our results demonstrate that PGP80 extracted with high-concentration ethanol exhibits stronger free radical scavenging activity at a lower molecular weight, confirming the hypothesis that smaller polysaccharides may have enhanced bioactivity [23].

Given its smaller molecular weight, higher carbohydrate content, and superior in vitro antioxidant activity, PGP80 was selected for further investigation of in vivo biological activities.

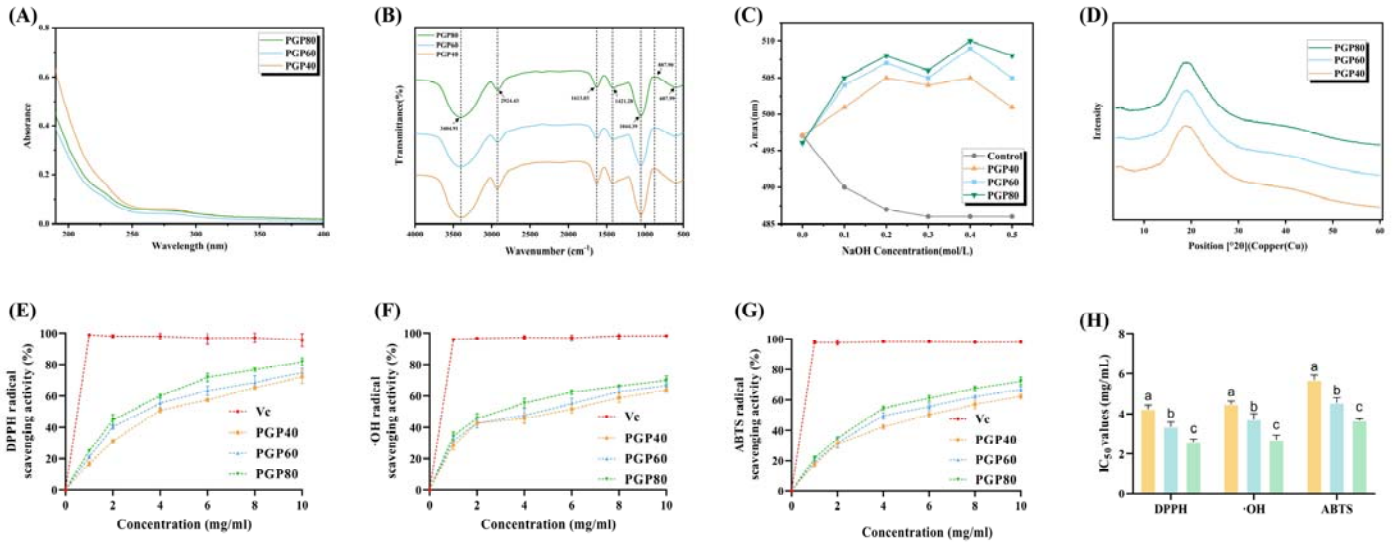

Figure 2: Structural characterization and antioxidant capacity of PGPs fractions. (A) UV-Vis absorption profiles. (B) FTIR spectral analysis. (C) Congo red binding assay for triple-helix conformation detection. (D) Crystalline structure by XRD. (E-G) Radical scavenging activities against DPPH, ·OH, and ABTS. (H) Comparative IC_{50} values of antioxidant effects Data are shown as mean ± S.D (n=6). One-way ANOVA was used, followed by post-hoc Tukey's test. The letters marked on the bar chart denote statistically significant differences ($P < 0.05$) among groups, whereas groups sharing the same letter are not significantly different ($P > 0.05$).

3.3 PGP80 improved the physiological and biochemical parameters in ALD mice

Body weight and liver index constitute essential parameters for monitoring pathological progression in ALD. The results indicated that body weight trajectories across experimental groups are presented in Fig. 3A. Comparative analysis revealed that the PGP80-H demonstrated an 11.57% reduction in body weight compared to the Mod ($P < 0.05$). While the PGP80-L, PGP80-M, and Pos exhibited not significant decreases of 6.56%, 8.57%, and 7.54% respectively relative to the Mod group, these differences did not reach statistical significance ($P > 0.05$, Fig. 3B). Fig. 3C revealed that the establishment of pathological model significantly elevated the liver index from 3.33% ± 0.32% (Con) to 4.41% ± 0.45% (Mod, $P < 0.05$). Notably, PGP80 intervention induced a dose dependent amelioration of hepatic hypertrophy, with all treatment groups showing statistically significant decrease compared to the Mod group ($P < 0.05$). Particularly, the high-dose group (PGP80-H) exhibited the most pronounced restoration of liver index (3.65% ± 0.29%) to physiological baseline, demonstrating statistical equivalence with the Con group ($P > 0.05$).

Fluctuations in serum levels of TC, TG, HDL-C, and LDL-C serve as critical biomarkers for assessing intrahepatic lipid deposition. As demonstrated in Fig.3F-I, TC and TG levels in the Mod group exhibited significant 128.14% and 65.21% increases compared to the Con group ($P < 0.05$), collectively indicating dysfunctional lipid homeostasis regulation. PGP80-H intervention induced marked reductions of 16.17% in TC and 33.55% in TG levels relative to the Mod group, demonstrating a favorable trend despite incomplete normalization to Con group baselines. Concurrently, PGP80-H administration improved lipid profiles through 37.93% elevation in HDL-C and 52.92% reduction in LDL-C compared to the Mod group ($P < 0.05$). Furthermore, measurement of hepatic TC and TG levels revealed that PGP80 intervention dose-dependently and significantly attenuates alcohol-induced pathological elevations in both hepatic TG and TC

(Supplementary Fig. S4). Especially in the PGP80-H group, liver TC and TG levels decreased by 31.49% and 19.64%, respectively, compared with the Mod group ($P < 0.05$). Previous studies confirm PGPs reduce hyperlipidemia via lowering body weight and serum lipids (TC/TG) in mice [31]. Our findings reveal that PGP80-H group improved body weight dynamics and serum lipid profiles (Fig.3B-I) compared to Mod group, likely due to PGP80's lipid-lowering capacity suppressing pathological metabolic dysregulation.

Serum ALT and AST, established biomarkers for hepatic injury assessment, exhibit fundamental associations with ALD pathological progression. Further analysis of hepatic function through ALT and AST assessment (Fig.3D-E) revealed that serum enzyme activities in Mod group mice increased significantly from 22.45±5.62 U/L (ALT) and 34.91±8.48 U/L (AST) in the Con group to 104.4±26.82 U/L (ALT) and 91.35±18.96 U/L (AST) ($P < 0.05$), demonstrating substantial alcohol-induced hepatic injury. High-dose PGP80 intervention markedly attenuated these elevations, reducing ALT and AST levels by 54.30% and 45.44% ($P < 0.05$) relative to the Mod group. Although the intervention efficacy of the PGP80-H group was slightly inferior to the Pos group, it still exhibited an inhibitory trend. Similarly, related studies have found that *Hypsizygus ulmarius* polysaccharides, owing to their significant antioxidant activity, can reduce hepatic AST and ALT levels as well as oxidative stress markers in mice with alcohol-induced liver injury [32]. These biochemical parameters demonstrate that PGP80 effectively counteracts alcohol-induced hepatocyte damage by regulating hepatocyte dysfunction and reducing lipid accumulation.

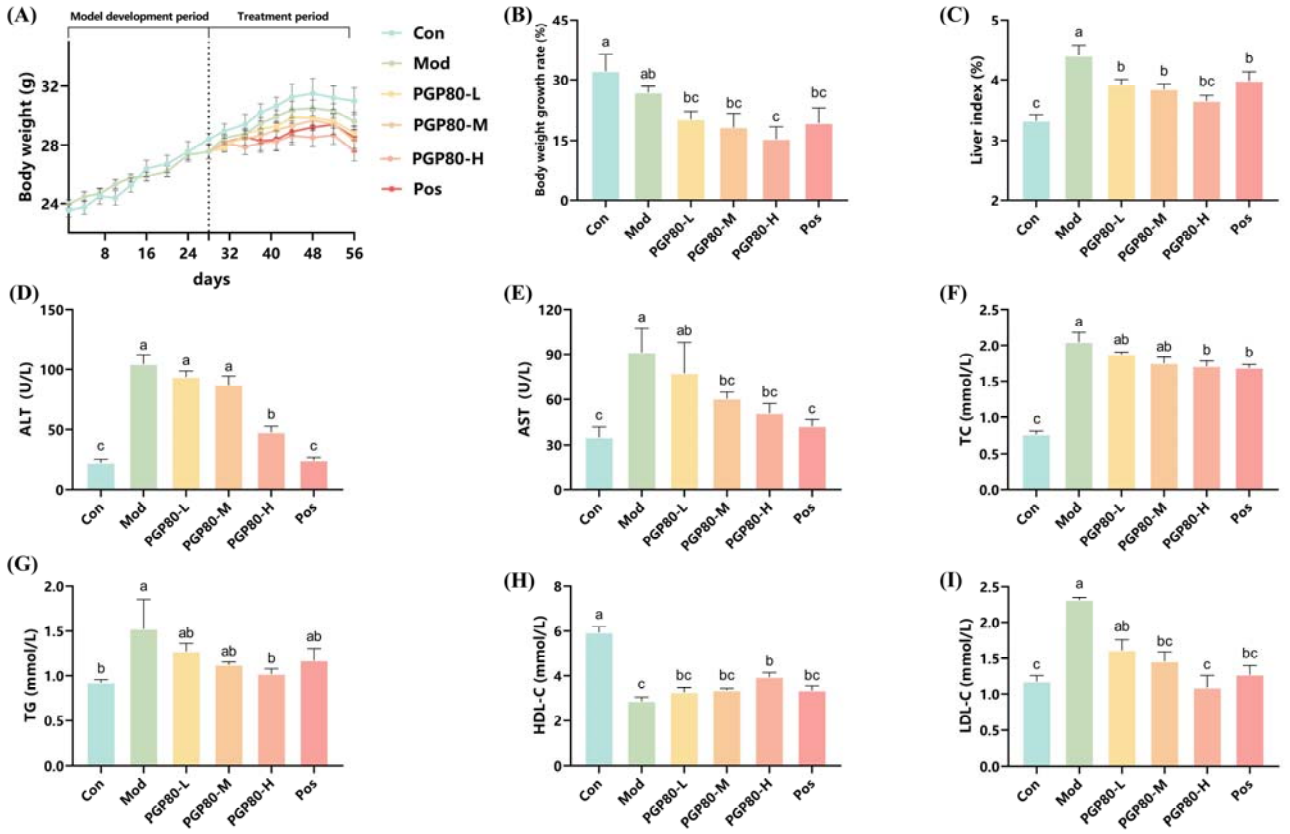

Figure 3: Effects of PGP80 on physiological and biochemical parameters in ALD mice. (A) Body weight. (B) Body weight gain at week 8 relative to week 0. (C) Liver index. (D–I) Serum levels of ALT, AST, TC, TG, HDL-C, and LDL-C. Data are shown as mean ± S.D (n=12). One-way ANOVA was used, followed by post-hoc Tukey's test. The letters marked on the bar chart denote statistically significant differences ($P < 0.05$) among groups, whereas groups sharing the same letter are not significantly different ($P > 0.05$).

3.4 PGP80 mitigates hepatic pathological manifestations and lipid accumulation

Hepatic tissues from each experimental groups were performed through microscopic observation of H&E sections at 200× magnification (Fig.4A). The Con group exhibited intact hepatic lobular architecture with regularly arranged hepatocytes demonstrating characteristic polygonal morphology. In contrast, the Mod group exhibited typical steatotic pathology, characterized by diffuse lipid vacuolization, disorganized lobular structure, marked hepatocellular swelling with focal disintegration, and extensive inflammatory cell infiltration. Particularly in the PGP80-H treatment group, hepatic tissues demonstrated nearly complete restoration of lobular architecture with orderly arranged polygonal hepatocytes. Minimal cellular swelling and lipid vacuoles were observed around central veins, along with well-defined intercellular matrix and absence of discernible inflammatory infiltration. The histological characteristics of PGP80-H group exhibited remarkable similarity to those observed in the Pos group.

Histological evaluation of Oil Red O-stained hepatic sections and quantitative analysis of stained areas are presented in Fig.4B-C. Hepatic tissues from the Con group demonstrated negligible lipid droplet deposition, whereas the Mod group exhibited dense accumulation of intensely stained lipid droplets, confirming impaired lipid metabolism in alcohol-induced liver disease models. Notably, PGP80 pretreatment substantially reduced both the quantity and density of lipid deposition in hepatic tissues compared to the Mod group.

3.5 PGP80 ameliorated the levels of oxidative stress markers, inflammatory factors, and alcohol metabolizing enzymes in ALD mice

Oxidative stress serves as a critical pathological factor in the progression of alcohol-induced liver injury due to ethanol metabolism in the liver triggering excessive generation of free radicals, thereby leading to a disruption of the redox system homeostasis. This oxidative stress is frequently accompanied by an inflammatory response, which represents a defense mechanism activated by the body to counteract cellular damage caused by ROS overproduction during oxidative stress [33]. Under alcohol intervention, the Mod group exhibited significant differences ($P < 0.05$) in oxidative stress markers (MDA, GSH, SOD), inflammatory factors (TNF-α, IL-1β), and alcohol-metabolizing enzymes (ADH, ALDH) compared to the Con group (Fig. 4D-J). Both PGP80 and bifendate treatments ameliorated alcohol-induced pathological alterations, including abnormal elevations of MDA, TNF-α, and IL-1β, as well as SOD reduction. Specifically, the PGP80-H group demonstrated 12.79%, 22.84%, and 21.31% decreases in MDA, TNF-α, and IL-1β levels respectively compared to Mod group ($P < 0.05$), accompanied by 24.96% and 22.89% increases in GSH and SOD activities. A dose-dependent patterns were observed in TNF-α, IL-1β, MDA, and SOD changes. Notably, while ADH and ALDH levels in Mod group showed significant reductions of 39.80% and 45.78% versus Con group ($P < 0.05$), PGP80 intervention exhibited no statistically significant improvement in ethanol-metabolizing enzyme activities ($P > 0.05$). A comparable study found that *Enteromorpha prolifera* polysaccharides significantly reduced oxidative stress levels. This protective effect worked by blocking the NF-κB pathway, which lowered the production of inflammatory factors in alcohol-fed mice [34]. These

findings align with our experimental observations that PGP80 treatment with equivalent antioxidant capacity improved liver injury markers, attenuated oxidative stress indicators, and suppressed inflammatory factors in ALD mice. Another study demonstrated that ADH and cytochrome P450 enzymes, under ethanol-induced oxidative stress conditions, metabolically produce acetaldehyde and reactive ROS. This metabolic shift compels the organism to deplete GSH as a defense mechanism [35], resulting in a dynamic negative correlation between ADH activity and systemic GSH levels. These results elucidate why PGP80 exhibits limited efficacy in ADH activation despite maintaining GSH homeostasis, suggesting that its protective mechanism against alcohol-induced liver injury may predominantly target oxidative stress mitigation rather than direct modulation of ethanol-metabolizing enzyme activities.

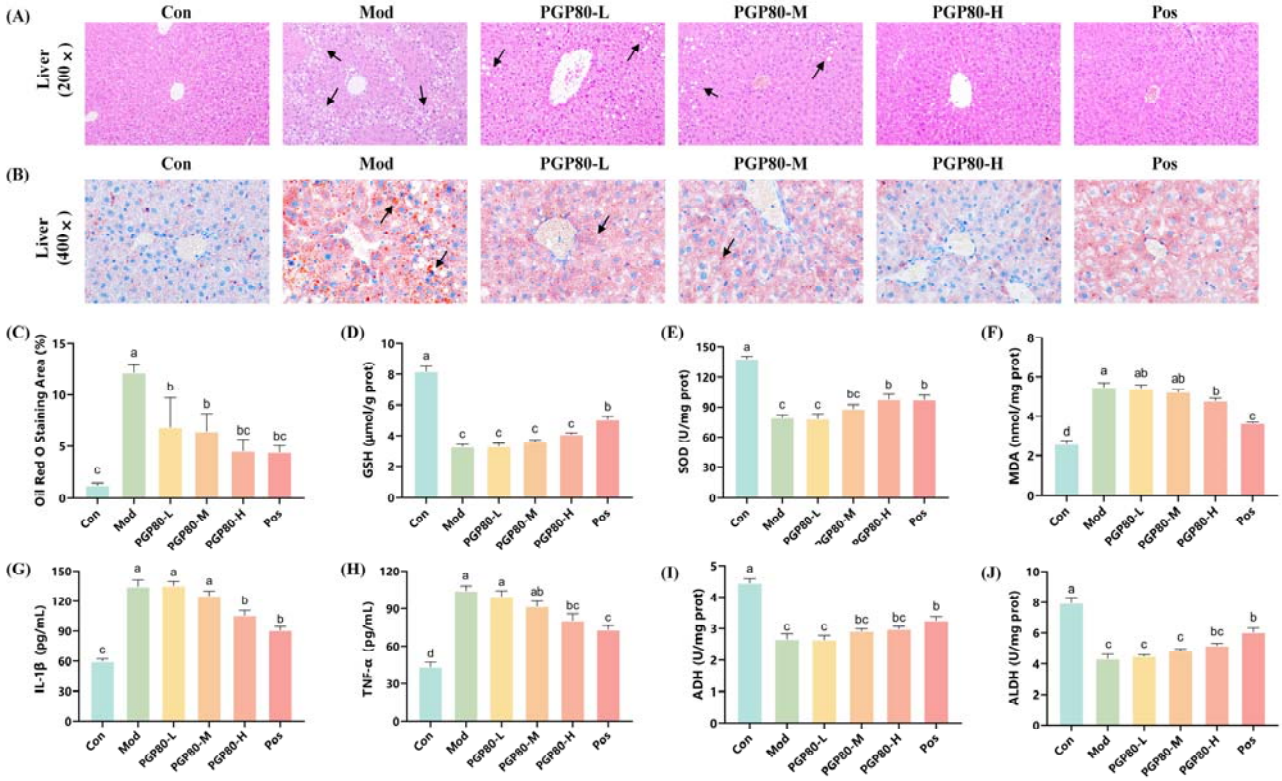

Figure 4: Effects of PGP80 on liver histopathology, oxidative Stress, inflammation, and alcohol metabolism in ALD Mice. (A) H&E-stained liver sections (200× magnification). (B) Oil Red O-stained liver sections (400× magnification). (C) Quantification of Oil Red O-positive lipid areas. (D–F) Hepatic oxidative stress markers: GSH, SOD, and MDA levels. (G–H) Serum pro-inflammatory cytokines: IL-1β and TNF-α levels. (I–J) Hepatic alcohol-metabolizing enzyme activities (ADH, ALDH). Data are shown as mean ± S.D (n=12). One-way ANOVA was used, followed by post-hoc Tukey's test. The letters marked on the bar chart denote statistically significant differences ($P < 0.05$) among groups, whereas groups sharing the same letter are not significantly different ($P > 0.05$).

3.6 PGP80 improves intestinal barrier integrity in ALD mice

Alcohol not only induces hepatic injury but also compromises intestinal epithelial integrity, resulting in elevated intestinal permeability and systemic release of bacterial endotoxin into the bloodstream [36]. As shown in Fig.5A-B, alcohol consumption significantly induced 164.72% and 113.64% elevations in serum LPS and D-lactic acid levels in the Mod group compared to the Con group ($p<0.05$). Notably, high-dose PGP80 treatment markedly reduced serum LPS and D-lactic acid concentrations by 14.96% and 40.46% versus the Mod group ($p<0.05$). Excessive ethanol intake has been demonstrated to disrupt intestinal barrier function, increasing intestinal permeability and elevating circulating levels of gut-derived endotoxins and

liver pro-inflammatory cytokines (IL-1β, TNF-α) [37]. Our observations support these findings, indicating potential mechanistic links between gut dysfunction and liver pathology.

The intestinal mucosal barrier, a crucial component of the digestive system, sustains both structural integrity and immune stability at the intestinal-environment interface. Specialized goblet cells produce mucins to establish a protective mucus layer, providing defense against pathogenic microorganisms and toxic agents while maintaining mucosal immune homeostasis [38]. Furthermore, natural bioactive polysaccharides have been reported to enhance mucin secretion through activation of intestinal goblet cells, promoting the formation of a hydrophobic mucus gel layer that effectively blocks invasive damage to intestinal epithelium by exogenous harmful substances [39]. In our study, H&E staining of ileal sections revealed that Con group mice maintained intact villi architecture with slender morphology and dense interstitial arrangement, whereas the Mod group exhibited disrupted villus integrity characterized by structural disorganization, villus fragmentation, length reduction, and decreased goblet cell numbers, indicating alcohol-induced intestinal barrier damage (Fig.5E). The various dose PGP80 intervention groups demonstrated morphological restoration, with Fig.5C showing a 40% increase in goblet cells in the PGP80-H group compared to Mod group. Notably, the Pos group exhibited limited efficacy in villous restoration with no statistically significant difference in goblet cell counts compared to the Mod group, which may be attributed to the target organ selectivity of the reference drug. In contrast, PGP80 demonstrated specific enteroprotective effects mediated by its unique spatial configuration and molecular modifications.

Intestinal tight junction proteins (Occludin and ZO-1) are essential for maintaining barrier integrity by regulating paracellular permeability. Their spatial stability and functional expression form the molecular basis of mucosal defense against pathogen/toxin translocation, while dynamic equilibrium mechanisms preserve barrier homeostasis [40]. The negative control images for IHC are presented in Supplementary Fig. S5, showing the absence of brown staining, indicating the specificity of the staining for all antibodies. IHC analysis of tight junction proteins Occludin and ZO-1 demonstrated extensive villus erosion and diminished staining intensity in the Mod group versus Con group (Fig.5F). Semi-quantitative H-Score analysis revealed PGP80 dose-dependently upregulated tight junction protein expression, with PGP80-H group showing 61.33% and 42.35% increases in Occludin and ZO-1 H-Scores compared to Mod group (Fig.5D). Moreover, the Western blot results exhibited concordance with the trends observed in IHC staining (Fig.5H). The expression of tight junction proteins in mouse ileum similarly demonstrated a significant dose-dependent effect following PGP80 intervention (Fig.5I-J). This mutual validation between the two experimental approaches collectively indicates that PGP80 administration ameliorates alcohol-induced impairment of intestinal barrier integrity. Natural polysaccharides protect intestinal health through integrated mechanisms, enhancing endogenous antioxidant enzymes to counteract oxidative stress while suppressing pro-inflammatory cytokine overexpression. These compounds simultaneously strengthen the epithelial barrier by upregulating tight junction proteins and maintain microbial equilibrium via structural modulation of gut microbiota [41]. These improvements in intestinal barrier integrity biomarkers suggest PGP80 may ameliorate ethanol-induced

barrier dysfunction by modulating intestinal permeability, thereby reducing endotoxin translocation and subsequent inflammatory responses.

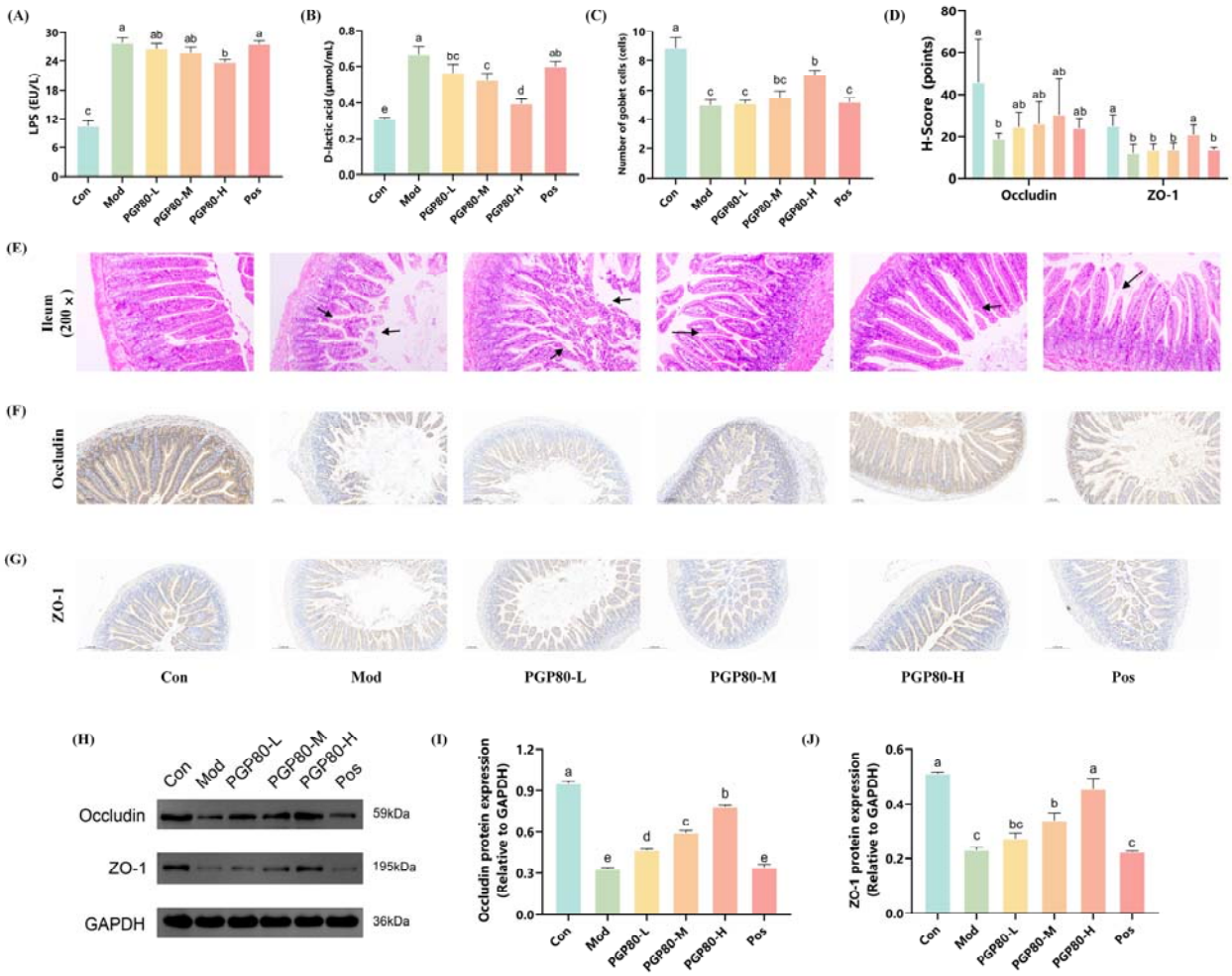

Figure 5: Effects of PGP80 on intestinal barrier integrity in ALD mice. (A–B) Serum levels of LPS and D-lactic acid. (C) Number of goblet cells in ileal villi. (D) Semi-quantitative H-score of tight junction protein expression. (E) H&E-stained ileal sections (200× magnification). (F–G) Immunohistochemical staining of ileal tight junction proteins Occludin and ZO-1 (200× magnification). (H) Western blot detection and quantitative data for (I) Occludin and (J) ZO-1. Data are shown as mean ± S.D (n=3-12, LPS and D-lactate measurements were performed with 12 biological replicates per group, while sectioning and Western blot were conducted with 3 biological replicates per group). One-way ANOVA was used, followed by post-hoc Tukey's test. The letters marked on the bar chart denote statistically significant differences (S0.05) among groups, whereas groups sharing the same letter are not significantly different ($P > 0.05$).

3.7 PGP80 modified the concentration of SCFAs in feces and serum

Accumulating evidence suggests that patients with ALD exhibit significant intestinal microbial metabolic dysregulation, predominantly characterized by abnormally elevated serum endotoxin levels and impaired SCFAs metabolism [42]. To investigate the effects of PGP80 on SCFAs metabolism in ALD mice through the gut-liver axis, GC was employed to conduct quantitative analysis of six principal SCFAs concentrations in fecal samples from different experimental groups (Fig.6A-F). Compared with the Con group, all experimental groups except the PGP80-H group exhibited significant reductions in six SCFAs concentrations ($P < 0.05$). Specifically, the Mod group showed 49.65%, 65.45%, and 78.42% decreases in acetic acid, propionic acid and butyric acid levels compared to the Con group, respectively, indicating that chronic ethanol exposure induces intestinal SCFAs metabolic disorders. Notably, high-dose PGP80

intervention significantly enhanced the biosynthesis of acetic acid, propionic acid and butyric acid in ALD mice, restoring these levels to 78.64%, 57.73%, and 69.71% of Con group's values, respectively. In order to more intuitively reflect the changing trend of SCFAs caused by alcohol and PGP80, the mean stacked column chart was con-ducted (Fig. 6G). The PGP80-H group demonstrated markedly elevated total SCFAs content compared to the Mod group. Analysis of SCFAs relative abundance revealed a substantial increase in butyric acid proportion (12.97%) in the PGP80-H group, reaching levels comparable to the Con group's butyric acid content (13.07%) (Fig. 6H).

Alcohol exposure can specifically inhibit the expression of the colonic epithelial monocarboxylate transporter (SMCT1), leading to impaired SCFA absorption and reduced blood concentrations. An increase in blood SCFA levels may indicate the restoration of intestinal epithelial function [43]. Our analysis of serum SCFA levels revealed that intervention with high-dose PGP80 significantly increased the concentrations of acetic acid (Fig.6I), propionic acid (Fig.6J), and butyric acid (Fig.6L) compared to the Mod group ($P < 0.05$). The high-dose PGP80 intervention simultaneously elevated total serum SCFAs content and increased the relative abundance of butyric acid in serum (Fig.6O-P). Collectively, these findings demonstrate that gut microbes utilize PGP80 to modulate SCFAs concentrations, thereby alleviating intestinal dysbiosis.

Existing studies suggest that natural polysaccharides may confer hepatoprotective effects through gut microbiota modulation – specifically by enhancing microbial diversity, elevating SCFAs production, and attenuating alcohol-induced hepatic lipid accumulation and oxidative stress via the gut-liver axis [44]. Notably, propionic acid and butyric acid can bind to GPR41/43 receptors, thereby activating the MAPK pathway and consequently accelerating the repair of intestinal epithelial cells while reducing the occurrence of intestinal leakage [45]. Meanwhile, butyric acid, as a histone deacetylase (HDAC) inhibitor, increases histone acetylation levels, thereby activating the expression of intestinal tight junction proteins and promoting mucin synthesis to maintain the intestinal barrier [46]. In our study, PGP80 administration significantly ameliorated alcohol-induced intestinal barrier hyperpermeability in ALD mice by promoting the secretion of SCFAs, particularly acetic acid, propionic acid and butyric acid (Fig.6), which are crucial for maintaining intestinal homeostasis and systemic metabolism [47]. This process upregulated tight junction protein expression, preserved intestinal barrier integrity, and reduced transmembrane translocation of endotoxins such as LPS and D-lactic acid (Fig.5). The monosaccharide composition analysis in this study revealed that PGP80 consists of a high proportion of Gal. Previous study indicate that polysaccharides with high galactose content are generally resistant to digestion by saliva and gastric juice but can be fermented by gut microbiota into SCFAs [48]. Furthermore, Wei et al. using an in vitro fermentation model, demonstrated that PGPs can be effectively utilized by *Faecalibacterium*, a primary butyrate-producing bacterium in the gut, thereby promoting the substantial production of SCFAs, particularly butyric acid. This finding aligns with our results from animal experiments, indicating the potential of PGPs as prebiotic candidates for food industry applications. [49].

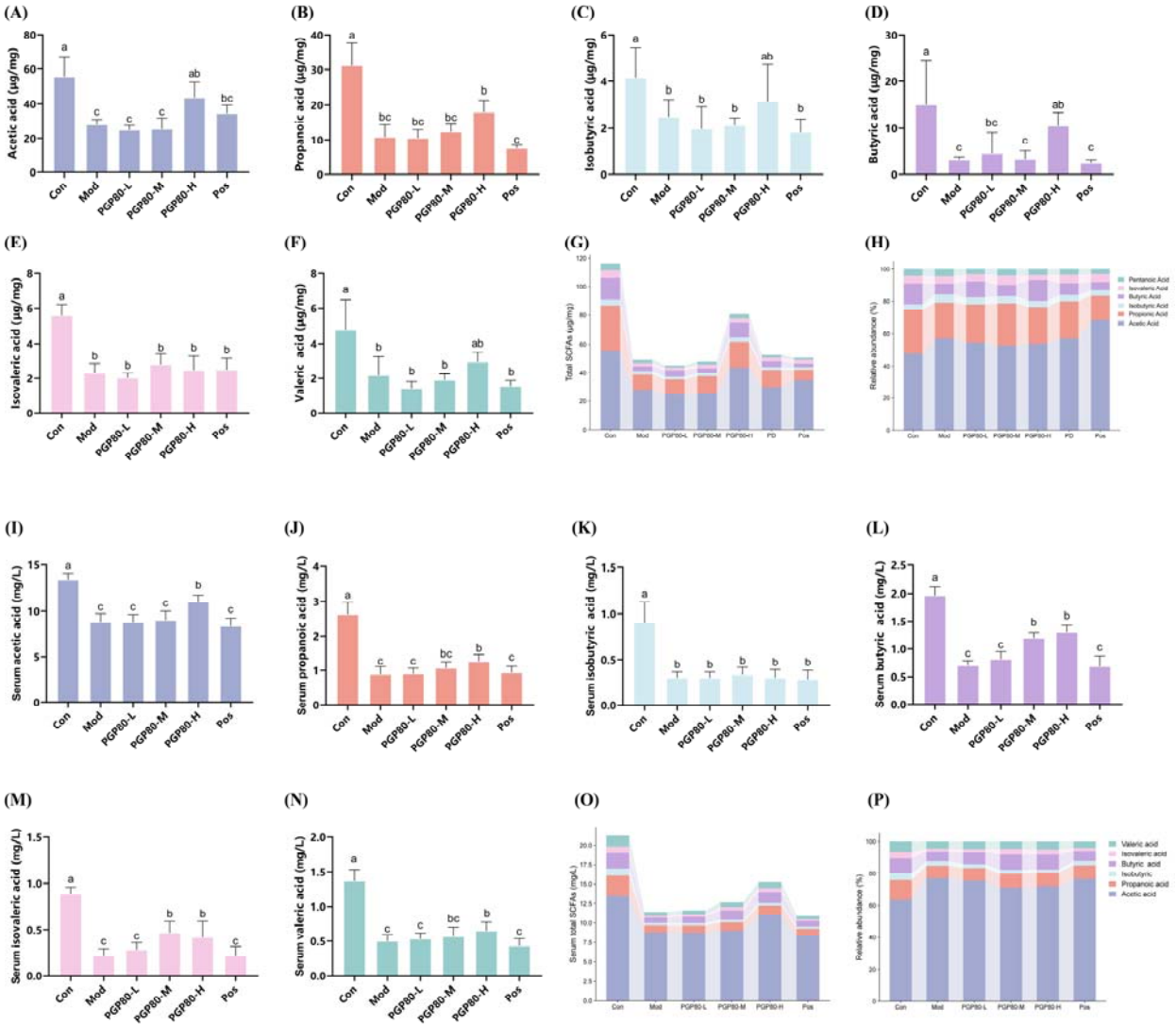

Figure 6: Effects of PGP80 on fecal and serum SCFAs in ALD mice. (A–F) Fecal concentrations of acetic acid, propionic acid, isobutyric acid, butyric acid, isovaleric acid, and valeric acid. (G) Fecal total SCFAs content. (H) Relative proportions of fecal individual SCFAs among experimental groups. (I–N) Serum concentrations of acetic acid, propionic acid, isobutyric acid, butyric acid, isovaleric acid, and valeric acid. (O) Serum total SCFAs content. (P) Relative proportions of serum individual SCFAs among experimental groups. Data are shown as mean ± S.D (n=6). One-way ANOVA was used, followed by post-hoc Tukey's test. The letters marked on the bar chart denote statistically significant differences ($P < 0.05$) among groups, whereas groups sharing the same letter are not significantly different ($P > 0.05$).

3.8 PGP80 treatment regulates gut microbial community structure of ALD mice

Based on preliminary experimental results, the subsequent gut microbiota study protocol was modified as follows: The positive control drug (bifendate) was excluded from further analysis due to its limited reference value for intestinal research, given that its primary pharmacological target is not the intestinal system. Meanwhile, the PGP80-H group demonstrated superior efficacy across all key parameters compared to other dosage groups, accompanied by dose-dependent positive effects, and was therefore selected as the experimental group for subsequent investigation.

16S rRNA sequencing of intestinal content samples was performed to investigate alcohol-induced perturbations in gut microbiota composition. Beta diversity analyses, including principal coordinate analysis (PCoA) and clustering dendrograms (Fig. 7A and B), revealed distinct microbial community segregation among the Mod, PGP80-H, and Con groups, demonstrating significant alcohol-related alterations in gut

microbiota architecture. Additionally, analysis of Alpha diversity using Shannon and Simpson indices (reflecting community diversity) revealed that alcohol intake significantly increased community diversity compared to the Con group, while high-dose PGP80 intervention further enhanced Alpha diversity (Fig. 7C and D). These findings substantiate the critical role of microbial dynamics in alcohol-related liver disease pathogenesis.

At the microbial phylum level, excessive alcohol consumption induced a marked elevation in the relative abundance of *Bacteroidota* and *Verrucomicrobiota* (Fig. 7E) while concurrently reducing *Bacillota* proportions (Fig. 7F). The Mod group manifested a significant decrease in the *Bacillota/Bacteroidota* ratio relative to the Con group, though administration of PGP80 effectively restored this balance (Fig. 7G). To elucidate key functional genera associated with alcohol metabolism and PGP80 responses in the gut microbiota of ALD mice, we performed comprehensive genus-level microbial profiling. The Upset plot analysis (Fig. 7H) demonstrated 93, 98, and 110 distinct bacterial genera in the Con, Mod, and PGP80-H groups respectively. Of these, 68 genera were conserved across all groups, with 13, 10, and 20 genera being exclusive to the Con, Mod, and PGP80-H groups correspondingly. These results demonstrate that alcohol and PGP80 interventions induced significant alterations in gut microbiota structure at the genus level in mice. LEfSe analysis revealed 45 differential microbial biomarkers among the experimental groups, distributed as 11 in Con, 3 in Mod, and 21 in PGP80-H (Fig. 7I-J). The Con group showed *Bacillota* predominance, particularly *Monoglobaceae*, *Monoglobus*, and *Intestinimonas* (LDA >3.0). Mod group microbiota exhibited characteristic enrichment of *Ruthenibacterium*, *Rikenella*, and *Roseburia* (LDA >3.0). The PGP80-H group exhibited substantial proliferation of *Dubosiella*, *Prevotellaceae_UCG-001*, *Ligilactobacillus*, and *Gordonibacter*, which emerged as core taxa (LDA >3.0) demonstrating ecological dominance within the microbial community. Following PGP80 intervention, pathobionts associated with intestinal disorders decreased while beneficial microorganisms linked to gut homeostasis increased, demonstrating PGP80's capacity to ameliorate alcohol-induced gut microbiota dysbiosis.

The gut microbiota serves as a pivotal regulator within the gut-liver axis, where microbial communities and their bioactive metabolites exert critical regulatory effects on intestinal barrier integrity and hepatic metabolic homeostasis. This intricate network of bidirectional communication is orchestrated through dual mechanisms which systemically influence disease progression [50]. Current studies demonstrate that excessive alcohol consumption exacerbates hepatic injury through gut microbiota homeostasis disruption via the gut-liver axis [51]. Patients with ALD exhibit significantly altered gut microbial diversity compared to healthy controls [52]. At the phylum level, alcohol exposure induces substantial reduction in *Bacillota* relative abundance concurrent with *Verrucomicrobiota* proliferation [53,54]. As a primary SCFAs producing taxa, *Bacillota* abundance positively correlates with intestinal SCFAs biosynthesis (particularly butyric acid), exerting restorative effects on gut barrier dysfunction through G protein-coupled receptor (GPCR) activation in enterocytes [55]. Furthermore, the *Bacillota*/*Bacteroidota* ratio serves as a critical indicator of microbial homeostasis, showing significant attenuation in ALD murine models [56]. Given these mechanistic

connections, microbiome-targeting interventions have gained prominence as a novel therapeutic paradigm for ALD management. Mechanistic insights from preclinical investigations have demonstrated that phytonutrient-rich dietary components exert hepatoprotective mechanisms through microbiota-mediated metabolic reprogramming [7]. For instance, polysaccharide derived from *Enteromorpha prolifera* modulates gut microbiota homeostasis by upregulating the relative abundance of *Bacillota* and increasing the *Bacillota*/*Bacteroidota* ratio. This intervention enhances SCFAs production, thereby reinforcing intestinal mucosal barrier integrity and reducing LPS translocation into systemic circulation. The subsequent decline in circulating LPS levels inactivates the NF-κB signaling pathway, ultimately suppressing inflammatory responses and conferring protection against ALD [34]. Consistent with these findings, our study demonstrated that PGP80 treatment modulates gut microbiota composition by increasing *Bacillota* abundance while reducing *Verrucomicrobia* in ALD mice (Fig.7E and F). Following PGP80 intervention, the *Bacillota*/*Bacteroidota* ratio demonstrated significant recovery compared to the Mod group (Fig.7G), which corresponded to elevated butyric acid levels observed in the PG80-H group through SCFAs analysis (Fig.6D), indicating improved restoration of intestinal microbiota homeostasis in ALD mice. According to LEfSe analysis, the dominant genera in the Mod group were *Ruthenibacterium* and *Rikenella* (Fig.7I). Current reports on *Ruthenibacterium* remain limited, with existing studies primarily suggesting that its elevated abundance may correlate with multiple sclerosis [57]. Furthermore, research has demonstrated that abnormal proportions of *Bacteroidota* in the gut microbiota of ALD patients alter SCFAs production, downregulate tight junction protein expression, increase intestinal barrier permeability, and exacerbate ALD progression through endotoxin leakage [58]. As a member of the *Bacteroidota* phylum, fluctuations in *Rikenella* abundance may reflect gut-liver axis disruption induced by this pathological process. After PGP80 intervention, *Dubosiella*, *Ligilactobacillus* and *Prevotellaceae_UCG-001* all major SCFAs-producing genera, became dominant in the intestinal microbiota of ALD mice (Fig.7I). Studies indicate that *Ligilactobacillus* and *Prevotellaceae_UCG-001* abundance positively correlates with propanoic acid and butyric acid levels, and they may remodel gut dysbiosis and enhance intestinal barrier function to inhibit inflammation by modulating SCFAs metabolism [59,60]. As a probiotic genus in the gut, increased relative abundance of *Ligilactobacillus* enhances the production of SCFAs, particularly propanoic acid, thereby restoring intestinal barrier integrity and mitigating alcohol-induced liver injury by suppressing LPS leakage [61]. Previous research indicates that an increased abundance of *Prevotellaceae_UCG-001* in the gut actively promotes SCFA production, which further alleviates the intestinal Th17/Treg imbalance and inflammatory response through crosstalk between the GPCR-HDAC3 and LPS-TLR4-NF-κB pathways, ultimately improving intestinal barrier function. [62]. *Dubosiella* enhances intestinal butyric acid biosynthesis, thereby alleviating gut barrier damage in colitis model mice [63]. Additionally, *Dubosiella* mediates exercise-induced amelioration of non-alcoholic fatty liver disease (NAFLD) in mice through the Fgf21-*Dubosiella* regulatory axis, with its abundance showing a significant positive correlation with reduced hepatic lipid deposition [64]. These findings align with our

experimental observations, demonstrating that high-dose PGP80 intervention elevates the abundance of these genera and improves their associated SCFAs, ultimately conferring protective effects against ALD.

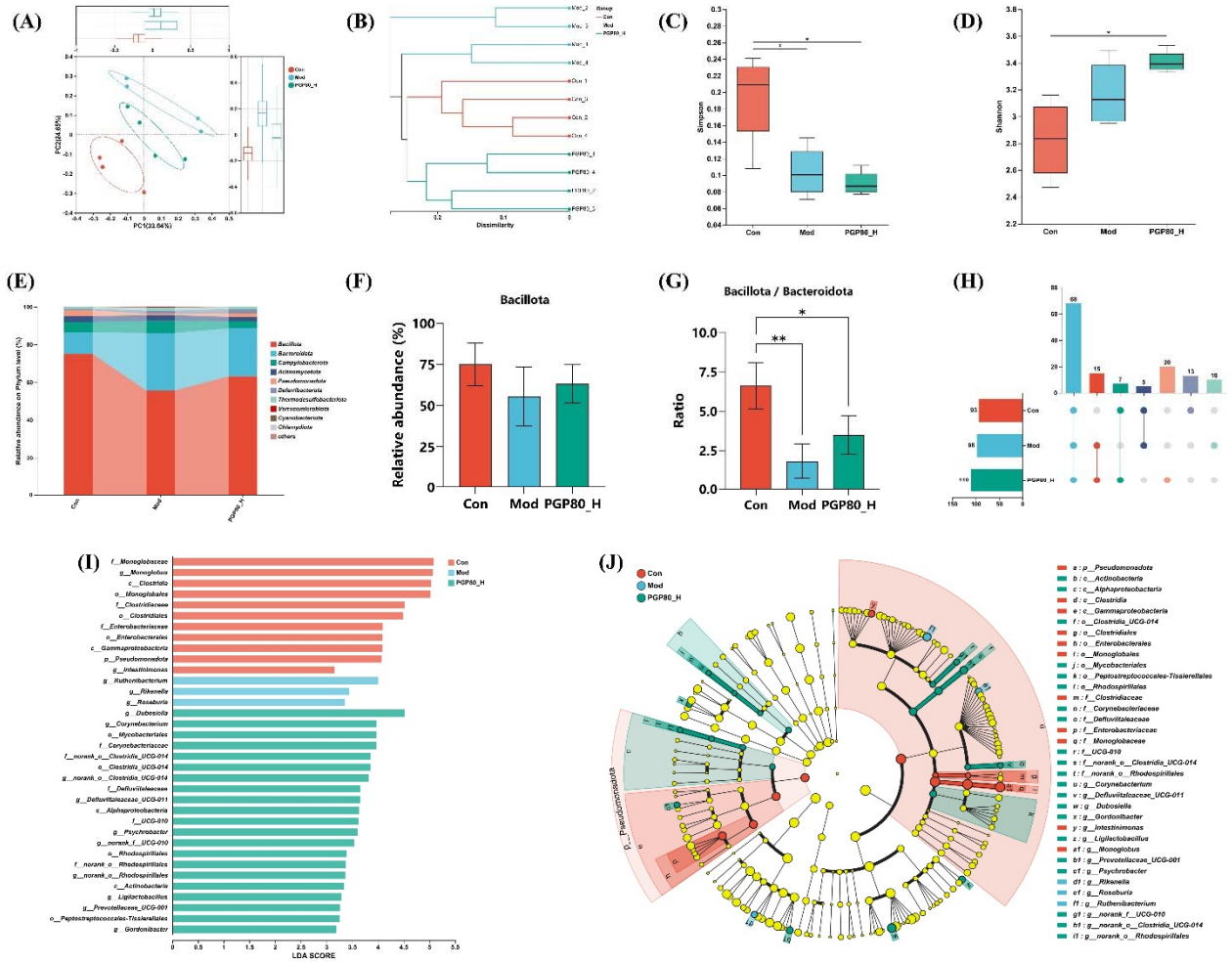

Figure 7: Effects of PGP80 on gut microbiota structure and homeostasis in ALD mice. (A) PCoA based on Bray-Curtis distance. (B) Hierarchical clustering tree. (C) Simpson diversity index. (D) Shannon diversity index. (E) Microbial distributions of different groups at the phylum level. (F) *Bacillota* abundance. (G) *Bacillota*/*Bacteroidota* ratio. (H) Upset plot showing genus-level taxa differences across groups. (I) LEfSe analysis: LDA scores of discriminative taxa (threshold >3). (J) LEfSe cladogram illustrating phylogenetic distribution of differential taxa. Data are shown as mean ± S.D (n=4). Statistical analysis was conducted using one-way analysis of variance (ANOVA), followed by post-hoc Tukey's test. * $P < 0.05$, ** $P < 0.01$.

3.9 Correlation of gut-liver characteristic indicators in ALD mice under PGP80 intervention

To investigate possible mechanisms underlying the gut-liver axis, we established a ternary correlation heatmap integrating characteristic gut microbiota, fecal SCFAs, and physiological/biochemical parameters. As shown in Fig.8, the dominant genera in the Mod group (*Ruthenibacterium*, *Rikenella*, and *Roseburia*) exhibited negative associations with SCFAs, particularly showing significant inverse correlations of *Ruthenibacterium* and *Rikenella* with acetic, propionic and butyric acid. In contrast, the predominant microbial taxa in the PGP80-H group (*Dubosiella*, *Ligilactobacillus* and *Prevotellaceae_UCG-001*) exhibited positive SCFAs correlations, notably strong positive relationships between *Dubosiella* and *Ligilactobacillus* with acetic, propionic and butyric acid. Correlation analysis between SCFAs and biochemical parameters revealed significant positive associations of acetic, propionic and butyric acid with ADH, ALDH, SOD, and

GSH, while demonstrating negative correlations with AST, ALT, and inflammatory factors like IL-6, TNF-α and LPS. PGP80 ameliorated alcohol-induced hepatic dysfunction and serum biochemical abnormalities in ALD mice through microbiota composition modulation and subsequent regulation of microbial metabolites including acetic, propionic and butyric acid.

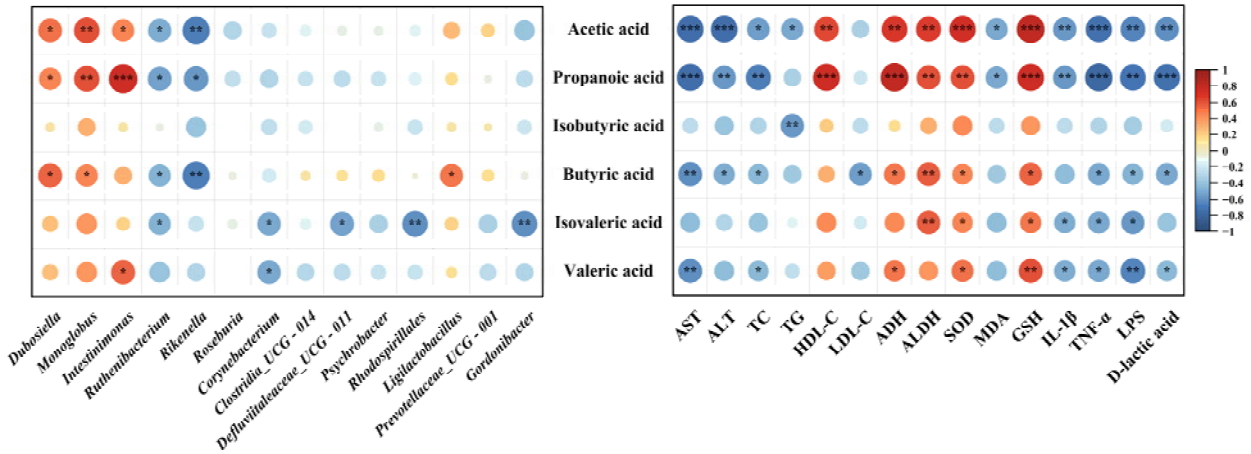

Figure 8: Spearman correlation analysis was conducted between key gut microbiota composition (genus level), fecal SCFAs, and serum biochemical parameters. P values were reported as $*P < 0.05$, $**P < 0.01$, and $***P < 0.001$. Circle size represents significance strength, red color represents positive correlation, and blue represents negative correlation.

Recent studies have increasingly demonstrated that gut microbiota can directly or indirectly regulate host metabolic pathways through microbial metabolites mediating intercellular signaling interactions [65]. These metabolites predominantly exist in low-molecular-weight forms, capable of crossing the intestinal mucosal barrier and being transported via systemic circulation to peripheral tissues, thereby achieving remote regulation of metabolic activities across multiple organs. Key microbially derived metabolites identified to date include endotoxins, secondary bile acids, and SCFAs , all of which exhibit significant dynamic alterations during the pathological progression of ALD [66]. In the correlation analysis of this study, the dominant bacterial genera in PGP80 (*Dubosiella*, *Ligilactobacillus*, and *Prevotellaceae_UCG-001*) exhibited positive correlations with SCFAs, while SCFAs were also positively associated with improvements in ALD-related biochemical markers (Fig.8). Collectively, PGP80 intervention reshaped the gut microbiota ecosystem by significantly enhancing the abundance of probiotic genera (*Dubosiella*, *Ligilactobacillus*, and *Prevotellaceae_UCG-001*) with SCFAs-synthesizing functions, while suppressing pathobionts such as *Rikenella* that abnormally proliferate under pathological conditions. This dynamic modulation of microbial communities enhanced the biosynthesis of SCFAs (predominantly acetic acid, propionic acid and butyric acid), consequently elevating tight junction protein (Occludin and Z0-1) expression while attenuating endotoxin leakage (notably LPS and D-lactic acid). PGP80 intervention may mediate these metabolic shifts through the gut-liver axis, alleviating oxidative stress and suppressing systemic inflammation, thus orchestrating multi-target protective mechanisms against alcohol-associated hepatic injury. (Fig.9).

However, this current study has not yet provided direct causal evidence demonstrating that the protective effect of PGP80 against ALD relies on the gut microbiota through germ-free mice or antibiotic-treated models. Furthermore, it lacks direct experimental evidence demonstrating the roles of the immune barrier and chemical barrier in ALD pathogenesis and during PGP80 intervention. Therefore, subsequent research should

prioritize validating the necessity of PGP80's amelioration of ALD mediated by the gut microbiota and systematically assess key immune barrier components, including but not limited to the secretory immunoglobulin A levels, the expression of antimicrobial peptides, regulatory cytokines within the gut mucosa, and markers of immune cell trafficking, thereby comprehensively evaluating gut-liver axis function.

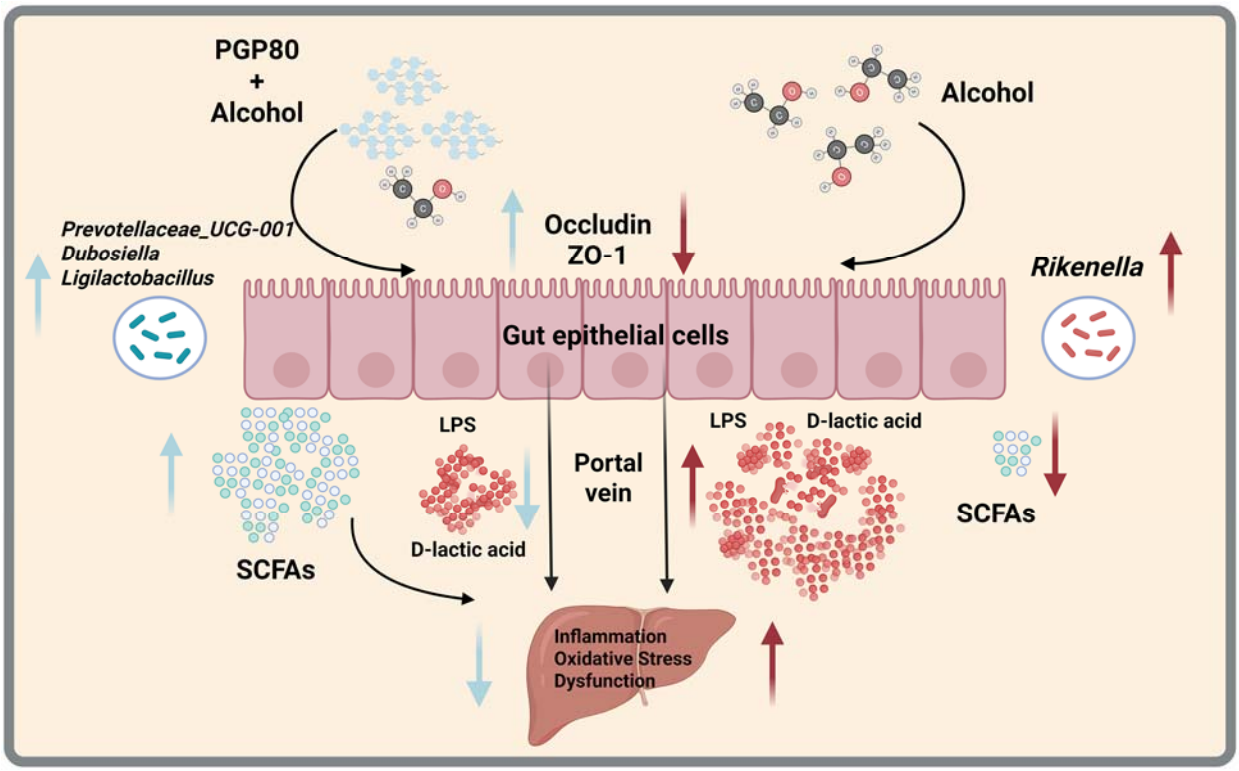

Figure 9: Potential mechanism of PGP80-mediated protection against alcoholic liver disease (ALD) through the gut-liver axis. PGP80 intervention reshaped the gut microbiota ecosystem in ALD mice by increasing the abundance of probiotic genera with SCFA-producing capabilities. This dynamic microbial modulation enhanced SCFAs biosynthesis, upregulated tight junction protein expression, and reduced endotoxin leakage. Through the gut-liver axis, these metabolic changes alleviated oxidative stress and suppressed systemic inflammation, thereby orchestrating multi-target protective effects against ALD.

4. Conclusion

In this study, three distinct PGPs fractions (PGP40, PGP60, and PGP80) were isolated from peach gum using a stepwise ethanol precipitation method. Preliminary characterization revealed that all three polysaccharide fractions are pyranose-type polysaccharides predominantly composed of arabinose and galactose with β-glycosidic linkages. Notably, PGP80 exhibited a smaller molecular weight and superior in vitro antioxidant activity compared to the other fractions. In vivo experiments demonstrated that PGP80 can significantly ameliorate liver steatosis, oxidative stress, and inflammatory responses induced by chronic alcohol consumption. Furthermore, analysis of SCFAs and gut microbiota in mouse fecal samples revealed that PGP80 promotes the growth of SCFA-producing bacterial taxa, maintains gut microbiota homeostasis, enhances SCFAs production, and restores alcohol-induced impairment of intestinal barrier integrity. By alleviating endotoxin leakage and modulating hepatic metabolic dysregulation through increased SCFAs levels, PGP80 exerts protective effects against alcohol-induced liver injury. In conclusion, dietary PGP80 alleviates alcohol-induced liver injury. This effect is associated with modulation of gut microbiome

composition and function, alongside changes in intestinal oxidative status and barrier integrity. These gut-related changes appear to contribute to the hepatoprotective activity observed with PGP80 supplementation. This study highlights PGP80's potential as a natural dietary component for supporting liver health against ALD, with the gut microbiota and SCFAs playing significant roles. Future research should verify the necessity of the gut microbiota for PGP80's benefits, elucidate specific SCFA pathways and structure-function relationships, and evaluate its effects in advanced liver injury models to expand its potential application value as a functional food.

Funding

This study was supported by the National Key Research and Development Program of China (No. 2022YFF1102500). Research Funding of Wuhan Polytechnic University NO. 53210052238 and Research and Innovation Initiatives of Wuhan Polytechnic University NO. 01500001.

Declaration of competing interest

The authors declare that they have no known competing financial interests or personal relationships that could have appeared to influence the work reported in this paper.

Data availability

Data will be made available on request.

Ethic approval and consent to participate

We declare that the ethical background to this study was approved by the ethical committee (Approval No. WPU202410008).

References

[1] W.B. Logge, K.C. Morley, P.S. Haber, A.J. Baillie, Executive Functioning Moderates Responses to Appetitive Cues: A Study in Severe Alcohol Use Disorder and Alcoholic Liver Disease, Alcohol and Alcoholism 54 (2019) 38–46. https://doi.org/10.1093/alcalc/agy083.

[2] B. Gao, R. Bataller, Alcoholic Liver Disease: Pathogenesis and New Therapeutic Targets, Gastroenterology 141 (2011) 1572–1585. https://doi.org/10.1053/j.gastro.2011.09.002.

[3] L. Gao, X. Chen, Z. Fu, J. Yin, Y. Wang, W. Sun, H. Ren, Y. Zhang, Kinsenoside Alleviates Alcoholic Liver Injury by Reducing Oxidative Stress, Inhibiting Endoplasmic Reticulum Stress, and Regulating AMPK-Dependent Autophagy, Front. Pharmacol. 12 (2022) 747325. https://doi.org/10.3389/fphar.2021.747325.

[4] L. Jiang, S. Lang, Y. Duan, X. Zhang, B. Gao, J. Chopyk, L.K. Schwanemann, M. Ventura-Cots, R. Bataller, F. Bosques-Padilla, E.C. Verna, J.G. Abraldes, R.S. Brown, V. Vargas, J. Altamirano, J. Caballería, D.L. Shawcross, S.B. Ho, A. Louvet, M.R. Lucey, P. Mathurin, G. Garcia-Tsao, T. Kisseleva, D.A. Brenner, X.M. Tu, P. Stärkel, D. Pride, D.E. Fouts, B. Schnabl, Intestinal Virome in Patients With Alcoholic Hepatitis, Hepatology 72 (2020) 2182–2196. https://doi.org/10.1002/hep.31459.

[5] X. Yan, X. Ren, X. Liu, Y. Wang, J. Ma, R. Song, X. Wang, Y. Dong, Q. Fan, J. Wei, A. Yu, G. She, Dietary Ursolic Acid Prevents Alcohol-Induced Liver Injury via Gut–Liver Axis Homeostasis Modulation: The Key Role of Microbiome Manipulation, J. Agric. Food Chem. 69 (2021) 7074–7083. https://doi.org/10.1021/acs.jafc.1c02362.

[6] H. Zhang, Y. Zuo, H. Zhao, H. Zhao, Y. Wang, X. Zhang, J. Zhang, P. Wang, L. Sun, H. Zhang, H. Liang, Folic acid ameliorates alcohol-induced liver injury via gut–liver axis homeostasis, Front. Nutr. 9 (2022) 989311. https://doi.org/10.3389/fnut.2022.989311.

[7] S. Teng, Y. Zhang, X. Jin, Y. Zhu, L. Li, X. Huang, D. Wang, Z. Lin, Structure and hepatoprotective activity of Usp10/NF-κB/Nrf2 pathway-related Morchella esculenta polysaccharide, Carbohydrate Polymers 303 (2023) 120453. https://doi.org/10.1016/j.carbpol.2022.120453.

[8] H.F. Qian, S.W. Cui, Q. Wang, C. Wang, H.M. Zhou, Fractionation and physicochemical characterization of peach gum polysaccharides, Food Hydrocolloids 25 (2011) 1285–1290. https://doi.org/10.1016/j.foodhyd.2010.09.027.

[9] C. Wei, P. He, L. He, X. Ye, J. Cheng, Y. Wang, W. Li, Y. Liu, Structure characterization and biological activities of a pectic polysaccharide from cupule of Castanea henryi, International Journal of Biological Macromolecules 109 (2018) 65–75. https://doi.org/10.1016/j.ijbiomac.2017.12.081.

[10] S. Zeng, J. Long, J. Sun, G. Wang, L. Zhou, A review on peach gum polysaccharide: Hydrolysis, structure, properties and applications, Carbohydrate Polymers 279 (2022) 119015. https://doi.org/10.1016/j.carbpol.2021.119015.

[11] X.-C. Yao, Y. Cao, S.-J. Wu, Antioxidant activity and antibacterial activity of peach gum derived oligosaccharides, International Journal of Biological Macromolecules 62 (2013) 1–3. https://doi.org/10.1016/j.ijbiomac.2013.08.022.

[12] S. Wu, M. Lu, S. Wang, Hypoglycaemic and hypolipidaemic properties of peach gum polysaccharides, 3 Biotech 7 (2017) 166. https://doi.org/10.1007/s13205-017-0852-0.

[13] B. Zhou, P. Liu, X. Yao, H. Cao, H. Zhu, Q. Wang, Y. Liu, M. Fang, Y. Wu, Z. Gong, Hepatoprotective effects of peach gum polysaccharides against alcoholic liver injury: moderation of oxidative stress and promotion of lipid metabolism, Front. Nutr. 10 (2024) 1325450. https://doi.org/10.3389/fnut.2023.1325450.

[14] Q. Lee, Z. Xue, Y. Luo, Y. Lin, M. Lai, H. Xu, B. Liu, M. Zheng, F. Lv, F. Zeng, Low molecular weight polysaccharide of Tremella fuciformis exhibits stronger antioxidant and immunomodulatory activities than high molecular weight polysaccharide, International Journal of Biological Macromolecules 281 (2024) 136097. https://doi.org/10.1016/j.ijbiomac.2024.136097.

[15] W. Xu, X.-J. Li, Y.-S. Zhong, J.-Q. He, W. Xie, Y.-K. Kang, H.-Z. Ying, C.-H. Yu, Structural characterizations and antiaging activities of hydrolyzed low-molecular-weight polysaccharides from Polygoni Multiflori Radix Praeparata, Carbohydrate Polymers 356 (2025) 123381. https://doi.org/10.1016/j.carbpol.2025.123381.

[16] J.-K. Yan, C. Wang, Y.-B. Yu, L.-X. Wu, T.-T. Chen, Z.-W. Wang, Physicochemical characteristics and in vitro biological activities of polysaccharides derived from raw garlic (Allium sativum L.) bulbs via three-phase partitioning combined with gradient ethanol precipitation method, Food Chemistry 339 (2021) 128081. https://doi.org/10.1016/j.foodchem.2020.128081.

[17] H. Fan, R. Li, Y. Zhang, X. Xu, S. Pan, F. Liu, Effect of H2O2/ascorbic acid degradation and gradient ethanol precipitation on the physicochemical properties and biological activities of pectin polysaccharides from Satsuma Mandarin, International Journal of Biological Macromolecules 280 (2024) 135843. https://doi.org/10.1016/j.ijbiomac.2024.135843.

[18] S. Govindan, A. Jayabal, J. Shanmugam, P. Ramani, Antioxidant and hepatoprotective effects of Hypsizygus ulmarius polysaccharide on alcoholic liver injury in rats, Food Science and Human Wellness 10 (2021) 523–535. https://doi.org/10.1016/j.fshw.2021.04.015.

[19] L. Wang, B. Zhang, J. Xiao, Q. Huang, C. Li, X. Fu, Physicochemical, functional, and biological properties of water-soluble polysaccharides from Rosa roxburghii Tratt fruit, Food Chemistry 249 (2018) 127–135. https://doi.org/10.1016/j.foodchem.2018.01.011.

[20] X. Wang, Y. Su, J. Su, J. Xue, R. Zhang, X. Li, Y. Li, Y. Ding, X. Chu, Optimization of Enzyme−Assisted Aqueous Extraction of Polysaccharide from Acanthopanax senticosus and Comparison of Physicochemical Properties and Bioactivities of Polysaccharides with Different Molecular Weights, Molecules 28 (2023) 6585. https://doi.org/10.3390/molecules28186585.

[21] A. Bertola, S. Mathews, S.H. Ki, H. Wang, B. Gao, Mouse model of chronic and binge ethanol feeding (the NIAAA model), Nat Protoc 8 (2013) 627–637. https://doi.org/10.1038/nprot.2013.032.

[22] M. Xu, J. Ren, Z. Jiang, S. Zhou, E. Wang, H. Li, W. Wu, X. Zhang, J. Wang, L. Jiao, Structural characterization and immunostimulant activities of polysaccharides fractionated by gradient ethanol precipitation method from Panax ginseng C. A. Meyer, Front. Pharmacol. 15 (2024) 1388206. https://doi.org/10.3389/fphar.2024.1388206.

[23] M. Duan, H. Shang, S. Chen, R. Li, H. Wu, Physicochemical properties and activities of comfrey polysaccharides extracted by different techniques, International Journal of Biological Macromolecules 115 (2018) 876–882. https://doi.org/10.1016/j.ijbiomac.2018.04.188.

[24] D. Yang, F. Lin, Y. Huang, J. Ye, M. Xiao, Separation, purification, structural analysis and immune-enhancing activity of sulfated polysaccharide isolated from sea cucumber viscera, International Journal of Biological Macromolecules 155 (2020) 1003–1018. https://doi.org/10.1016/j.ijbiomac.2019.11.064.

[25] Q. Li, W. Wang, Y. Zhu, Y. Chen, W. Zhang, P. Yu, G. Mao, T. Zhao, W. Feng, L. Yang, X. Wu, Structural elucidation and antioxidant activity a novel Se-polysaccharide from Se-enriched Grifola frondosa, Carbohydrate Polymers 161 (2017) 42–52. https://doi.org/10.1016/j.carbpol.2016.12.041.

[26] Y.-T. Wu, Y.-F. Huo, L. Xu, Y.-Y. Xu, X.-L. Wang, T. Zhou, Purification, characterization and antioxidant activity of polysaccharides from Porphyra haitanensis, International Journal of Biological Macromolecules 165 (2020) 2116–2125. https://doi.org/10.1016/j.ijbiomac.2020.10.053.

[27] R. Hashemifesharaki, E. Xanthakis, Z. Altintas, Y. Guo, S.M.T. Gharibzahedi, Microwave-assisted extraction of polysaccharides from the marshmallow roots: Optimization, purification, structure, and bioactivity, Carbohydrate Polymers 240 (2020) 116301. https://doi.org/10.1016/j.carbpol.2020.116301.

[28] H. Huang, G. Huang, Extraction, separation, modification, structural characterization, and antioxidant activity of plant polysaccharides, Chem Biol Drug Des 96 (2020) 1209–1222. https://doi.org/10.1111/cbdd.13794.

[29] R. Guo, L. Ai, N. Cao, J. Ma, Y. Wu, J. Wu, X. Sun, Physicochemical properties and structural characterization of a galactomannan from Sophora alopecuroides L. seeds, Carbohydrate Polymers 140 (2016) 451–460. https://doi.org/10.1016/j.carbpol.2015.12.058.

[30] G. Ren, L. Xu, T. Lu, J. Yin, Structural characterization and antiviral activity of lentinan from Lentinus edodes mycelia against infectious hematopoietic necrosis virus, International Journal of Biological Macromolecules 115 (2018) 1202–1210. https://doi.org/10.1016/j.ijbiomac.2018.04.132.

[31] S. Wu, M. Lu, S. Wang, Hypoglycaemic and hypolipidaemic properties of peach gum polysaccharides, 3 Biotech 7 (2017) 166. https://doi.org/10.1007/s13205-017-0852-0.

[32] S. Govindan, A. Jayabal, J. Shanmugam, P. Ramani, Antioxidant and hepatoprotective effects of Hypsizygus ulmarius polysaccharide on alcoholic liver injury in rats, Food Science and Human Wellness 10 (2021) 523–535. https://doi.org/10.1016/j.fshw.2021.04.015.

[33] M. Monserrat-Mesquida, M. Quetglas-Llabrés, X. Capó, C. Bouzas, D. Mateos, A. Pons, J.A. Tur, A. Sureda, Metabolic Syndrome Is Associated with Oxidative Stress and Proinflammatory State, Antioxidants 9 (2020) 236. https://doi.org/10.3390/antiox9030236.

[34] T. Yan, J. Sun, Y. Zhang, C. Wen, J. Yang, *Enteromorpha prolifera* Polysaccharide Alleviates Acute Alcoholic Liver Injury in C57 BL/6 Mice through the Gut–Liver Axis and NF-κB Pathway, J. Agric. Food Chem. 72 (2024) 23258–23270. https://doi.org/10.1021/acs.jafc.4c05262.

[35] Y. Jiang, T. Zhang, P. Kusumanchi, S. Han, Z. Yang, S. Liangpunsakul, Alcohol Metabolizing Enzymes, Microsomal Ethanol Oxidizing System, Cytochrome P450 2E1, Catalase, and Aldehyde Dehydrogenase in Alcohol-Associated Liver Disease, Biomedicines 8 (2020) 50. https://doi.org/10.3390/biomedicines8030050.

[36] T. Shao, C. Zhao, F. Li, Z. Gu, L. Liu, L. Zhang, Y. Wang, L. He, Y. Liu, Q. Liu, Y. Chen, H. Donde, R. Wang, V.R. Jala, S. Barve, S.-Y. Chen, X. Zhang, Y. Chen, C.J. McClain, W. Feng, Intestinal HIF-1α deletion exacerbates alcoholic liver disease by inducing intestinal dysbiosis and barrier dysfunction, Journal of Hepatology 69 (2018) 886–895. https://doi.org/10.1016/j.jhep.2018.05.021.

[37] S. Bala, M. Marcos, A. Gattu, D. Catalano, G. Szabo, Acute Binge Drinking Increases Serum Endotoxin and Bacterial DNA Levels in Healthy Individuals, PLoS ONE 9 (2014) e96864. https://doi.org/10.1371/journal.pone.0096864.

[38] J. Wang, M. He, M. Yang, X. Ai, Gut microbiota as a key regulator of intestinal mucosal immunity, Life Sciences 345 (2024) 122612. https://doi.org/10.1016/j.lfs.2024.122612.

[39] S. Hino, K. Sonoyama, H. Bito, H. Kawagishi, S. Aoe, T. Morita, Low-Methoxyl Pectin Stimulates Small Intestinal Mucin Secretion Irrespective of Goblet Cell Proliferation and Is Characterized by Jejunum Muc2 Upregulation in Rats, The Journal of Nutrition 143 (2013) 34–40. https://doi.org/10.3945/jn.112.167064.

[40] J. Xiao, R. Zhang, Y. Wu, C. Wu, X. Jia, L. Dong, L. Liu, Y. Chen, Y. Bai, M. Zhang, Rice Bran Phenolic Extract Protects against Alcoholic Liver Injury in Mice by Alleviating Intestinal Microbiota Dysbiosis, Barrier Dysfunction, and Liver Inflammation Mediated by the Endotoxin–TLR4–NF-κB Pathway, J. Agric. Food Chem. 68 (2020) 1237–1247. https://doi.org/10.1021/acs.jafc.9b04961.

[41] C. Tang, R. Ding, J. Sun, J. Liu, J. Kan, C. Jin, The impacts of natural polysaccharides on intestinal microbiota and immune responses – a review, Food Funct. 10 (2019) 2290–2312. https://doi.org/10.1039/C8FO01946K.

[42] S.K. Sarin, A. Pande, B. Schnabl, Microbiome as a therapeutic target in alcohol-related liver disease, Journal of Hepatology 70 (2019) 260–272. https://doi.org/10.1016/j.jhep.2018.10.019.

[43] P. Chen, M. Torralba, J. Tan, M. Embree, K. Zengler, P. Stärkel, J.-P. Van Pijkeren, J. DePew, R. Loomba, S.B. Ho, J.S. Bajaj, E.A. Mutlu, A. Keshavarzian, H. Tsukamoto, K.E. Nelson, D.E. Fouts, B. Schnabl, Supplementation of Saturated Long-Chain Fatty Acids Maintains Intestinal Eubiosis and Reduces Ethanol-induced Liver Injury in Mice, Gastroenterology 148 (2015) 203-214.e16. https://doi.org/10.1053/j.gastro.2014.09.014.

[44] Y. Zhang, J. Liu, S. Xu, M. Luo, S. Yang, S. Yu, Structural characterization of *Aspalatus linearis* polysaccharide and its improving effect on acute alcoholic liver injury, Journal of Food Science 89 (2024) 4535–4550. https://doi.org/10.1111/1750-3841.17055.

[45] G. Tolhurst, H. Heffron, Y.S. Lam, H.E. Parker, A.M. Habib, E. Diakogiannaki, J. Cameron, J. Grosse, F. Reimann, F.M. Gribble, Short-Chain Fatty Acids Stimulate Glucagon-Like Peptide-1 Secretion via the G-Protein–Coupled Receptor FFAR2, Diabetes 61 (2012) 364–371. https://doi.org/10.2337/db11-1019.

[46] J.R. Davie, Inhibition of Histone Deacetylase Activity by Butyrate, The Journal of Nutrition 133 (2003) 2485S-2493S. https://doi.org/10.1093/jn/133.7.2485S.

[47] Y. Yao, X. Cai, W. Fei, Y. Ye, M. Zhao, C. Zheng, The role of short-chain fatty acids in immunity, inflammation and metabolism, Critical Reviews in Food Science and Nutrition 62 (2022) 1–12. https://doi.org/10.1080/10408398.2020.1854675.

[48] X. Lin, B. Xiao, J. Liu, M. Cao, Z. Yang, L. Zhao, G. Chen, An acidic heteropolysaccharide rich in galactose and arabinose derived from ginger: Structure and dynamics, Food Bioscience 56 (2023) 103127. https://doi.org/10.1016/j.fbio.2023.103127.

[49] C. Wei, L. Yao, L. Zhang, Y. Zhang, Q. Luo, S. Qiu, X. Zeng, S. Chen, X. Ye, In Vitro Digestion and Fecal Fermentation of Peach Gum Polysaccharides with Different Molecular Weights and Their Impacts on Gut Microbiota, Foods 11 (2022) 3970. https://doi.org/10.3390/foods11243970.

[50] X. Wang, H. Chen, W. Zhu, Z. Wang, Y. Pan, Y. Sun, H. Xiong, J. Zhou, W. Cheng, K. Cheng, Akebia trifoliata extracts attenuate liver injury via gut–liver axis in a murine model of nonalcoholic fatty liver disease with low-grade colitis, Food Research International 208 (2025) 116202. https://doi.org/10.1016/j.foodres.2025.116202.

[51] F. Yang, X. Li, J. Sun, X. Pang, Q. Sun, Y. Lu, Regulatory mechanisms of the probiotic-targeted gut–liver axis for the alleviation of alcohol-related liver disease: a review, Critical Reviews in Food Science and Nutrition (2025) 1–22. https://doi.org/10.1080/10408398.2025.2455954.

[52] X.-M. Zhang, Y.-C. Huang, B.-Z. Chen, Q. Li, P.-P. Wu, W.-H. Chen, R.-H. Wu, C. Li, Water decoction of Pericarpium citri reticulatae and Amomi fructus ameliorates alcohol-induced liver disease involved in the modulation of gut microbiota and TLR4/NF-κB pathway, Front. Pharmacol. 15 (2024) 1392338. https://doi.org/10.3389/fphar.2024.1392338.

[53] A.W. Yan, D.E. Fouts, J. Brandl, P. Stärkel, M. Torralba, E. Schott, H. Tsukamoto, K.E. Nelson, D.A. Brenner, B. Schnabl, Enteric dysbiosis associated with a mouse model of alcoholic liver disease, Hepatology 53 (2011) 96–105. https://doi.org/10.1002/hep.24018.

[54] X. Geng, M. Zhuang, W. Tian, H. Shang, Z. Gong, Y. Lv, J. Li, Green Radish Polysaccharide Prevents Alcoholic Liver Injury by Interfering with Intestinal Bacteria and Short-Chain Fatty Acids in Mice, Foods 13 (2024) 3733. https://doi.org/10.3390/foods13233733.

[55] S. Zhang, J. Zhao, F. Xie, H. He, L.J. Johnston, X. Dai, C. Wu, X. Ma, Dietary fiber-derived short-chain fatty acids: A potential therapeutic target to alleviate obesity-related nonalcoholic fatty liver disease, Obesity Reviews 22 (2021) e13316. https://doi.org/10.1111/obr.13316.

[56] L. Bull-Otterson, W. Feng, I. Kirpich, Y. Wang, X. Qin, Y. Liu, L. Gobejishvili, S. Joshi-Barve, T. Ayvaz, J. Petrosino, M. Kong, D. Barker, C. McClain, S. Barve, Metagenomic Analyses of Alcohol Induced Pathogenic Alterations in the Intestinal Microbiome and the Effect of Lactobacillus rhamnosus GG Treatment, PLoS ONE 8 (2013) e53028. https://doi.org/10.1371/journal.pone.0053028.

[57] X. Zhou, R. Baumann, X. Gao, M. Mendoza, S. Singh, I. Katz Sand, Z. Xia, L.M. Cox, T. Chitnis, H. Yoon, L. Moles, S.J. Caillier, A. Santaniello, G. Ackermann, A. Harroud, R. Lincoln, R. Gomez, A. González Peña, E. Digga, D.J. Hakim, Y. Vazquez-Baeza, K. Soman, S. Warto, G. Humphrey, M. Farez, L.A. Gerdes, J.R. Oksenberg, S.S. Zamvil, S. Chandran, P. Connick, D. Otaegui, T. Castillo-Triviño, S.L. Hauser, J.M. Gelfand, H.L. Weiner, R. Hohlfeld, H. Wekerle, J. Graves, A. Bar-Or, B.A.C. Cree, J. Correale, R. Knight, S.E. Baranzini, Gut microbiome of multiple sclerosis patients and paired household healthy controls reveal associations with disease risk and course, Cell 185 (2022) 3467-3486.e16. https://doi.org/10.1016/j.cell.2022.08.021.

[58] P. Hartmann, C.T. Seebauer, B. Schnabl, Alcoholic Liver Disease: The Gut Microbiome and Liver Cross Talk, Alcoholism Clin & Exp Res 39 (2015) 763–775. https://doi.org/10.1111/acer.12704.

[59] S. Yang, G. Liu, X. Xia, D. Gan, S. Xiang, M. Xiang, α-Mangostin suppresses ethanol-induced gastric ulceration by regulating the Nrf2/HO-1 and NF-κB/NLRP3/caspase-1 signaling pathways and gut microbiota, Heliyon 10 (2024) e24339. https://doi.org/10.1016/j.heliyon.2024.e24339.

[60] Y. Wan, F. Wang, J. Yuan, J. Li, D. Jiang, J. Zhang, H. Li, R. Wang, J. Tang, T. Huang, J. Zheng, A.J. Sinclair, J. Mann, D. Li, Effects of dietary fat on gut microbiota and faecal metabolites, and their relationship with cardiometabolic risk factors: a 6-month randomised controlled-feeding trial, Gut 68 (2019) 1417–1429. https://doi.org/10.1136/gutjnl-2018-317609.

[61] M. Tao, Y. Xie, X. Fan, X. Yan, W. Fan, R. Cao, M. Li, R. Li, L. Wang, Neutral polysaccharide from Dendrobium officinale alleviates acute alcohol-induced liver injury via the gut microbiota−short chain fatty acids−liver axis, International Journal of Biological Macromolecules 317 (2025) 144719. https://doi.org/10.1016/j.ijbiomac.2025.144719.

[62] N. Wang, Y. Dilixiati, L. Xiao, H. Yang, Z. Zhang, Different Short-Chain Fatty Acids Unequally Modulate Intestinal Homeostasis and Reverse Obesity-Related Symptoms in Lead-Exposed High-Fat Diet Mice, J. Agric. Food Chem. 72 (2024) 18971–18985. https://doi.org/10.1021/acs.jafc.4c04193.

[63] F. Wan, H. Han, R. Zhong, M. Wang, S. Tang, S. Zhang, F. Hou, B. Yi, H. Zhang, Dihydroquercetin supplement alleviates colonic inflammation potentially through improved gut microbiota community in mice, Food Funct. 12 (2021) 11420–11434. https://doi.org/10.1039/D1FO01422F.

[64] X. Ye, P. Sun, S. Lao, M. Wen, R. Zheng, Y. Lin, L. Gan, X. Fan, P. Wang, Z. Li, X. Yan, L. Zhao, Fgf21-Dubosiella axis mediates the protective effects of exercise against NAFLD development, Life Sciences 334 (2023) 122231. https://doi.org/10.1016/j.lfs.2023.122231.

[65] N. Fornelos, E.A. Franzosa, J. Bishai, J.W. Annand, A. Oka, J. Lloyd-Price, T.D. Arthur, A. Garner, J. Avila-Pacheco, H.J. Haiser, A.C. Tolonen, J.A. Porter, C.B. Clish, R.B. Sartor, C. Huttenhower, H. Vlamakis, R.J. Xavier, Growth effects of N-acylethanolamines on gut bacteria reflect altered bacterial abundances in inflammatory bowel disease, Nat Microbiol 5 (2020) 486–497. https://doi.org/10.1038/s41564-019-0655-7.

[66] J.S. Bajaj, Alcohol, liver disease and the gut microbiota, Nat Rev Gastroenterol Hepatol 16 (2019) 235–246. https://doi.org/10.1038/s41575-018-0099-1.